Inorganic Chemistry Communications 176 (2025) 114274

Contents lists available at ScienceDirect

Inorganic Chemistry Communications

journal homepage: www.elsevier.com/locate/inoche

# Synthesis, characterization, and photocatalytic efficiency of Mg-doped ZnO nanoparticles for basic Fuchsin dye degradation: Experimental and theoretical insights

Farida Khammar [a,b], Said Boukerche [c,d,*], Selma Djaber [c], Abir Boublia [e], Abdessalam Messabhia [f,g], Amel Gharbi [h], Hana Ferkous [i,j], Cristian Vacacela Gomez [k], Stefano Bellucci [k,l], Malik Albrahim [m], Manawwer Alam [n], Yacine Benguerba [o,**]

[a] Department of Mechanical Engineering, Faculty of Science and Technology, University Mohamed Cherif Messaadia of Souk Ahras, 41000, Algeria
[b] Laboratory of Research on Electromechanical and Dependability (LRESF), University Mohamed Cherif Messaadia of Souk Ahras, 41000, Algeria
[c] Department of Matter Sciences, Faculty of Science and Technology, University Mohamed Cherif Messaadia of Souk Ahras, 41000, Algeria
[d] Laboratory of Water and Environment Sciences and Technology (LST2E), University Mohamed Cherif Messaadia of Souk Ahras, 41000, Algeria
[e] Université de Lorraine, CNRS, L2CM, F-54000 Nancy, France
[f] Department of Chemical Engineering, Faculty of Science and Technology, University Mohamed Cherif Messaadia of Souk Ahras, 41000, Algeria
[g] Laboratory of Physics of Matter and Radiation, Faculty of Science and Technology, University Mohamed Cherif Messaadia of Souk Ahras, 41000, Algeria
[h] Research Center in Industrial Technologies CRTI, Algiers, Algeria
[i] Department of Technology, University of 20 August 1955, 21000 Skikda, Algeria
[j] Laboratory of Mechanical Engineering and Materials, Faculty of Technology, University of 20 August 1955, 21000 Skikda, Algeria
[k] INFN-Laboratori Nazionali di Frascati, Via E. Fermi 54, 00044 Frascati, Italy
[l] Laboratory of Optical Processes in Nanostructured Materials, National Institute of Materials Physics, P.O. Box MG-7, R077125 Bucharest, Romania
[m] Chemical Engineering Department, College of Engineering, University of Ha'il, Ha'il 81441, Saudi Arabia
[n] Department of Chemistry, College of Science, King Saud University, PO Box 2455, Riyadh 11451, Saudi Arabia
[o] Laboratoire de Biopharmacie Et Pharmacotechnie (LPBT), Université Ferhat ABBAS Sétif-1, Sétif 19000, Algeria

ARTICLE INFO

*Keywords:*
Mg-doped ZnO nanoparticles
Characterization
Photocatalysis
Basic Fuchsin
DFT
RDG
QTAIM
Wastewater treatment

ABSTRACT

This study synthesized Mg-doped ZnO nanoparticles using the co-precipitation method with doping concentrations ranging from 2 % to 8 %. The structural, morphological, and optical properties of the synthesized nanoparticles were systematically characterized using X-ray diffraction (XRD), scanning electron microscopy (SEM), Fourier-transform infrared spectroscopy (FTIR), and UV–Visible spectroscopy. XRD analysis confirmed the successful incorporation of $Mg^{2+}$ ions into the ZnO lattice, evidenced by lattice parameter shifts and a significant reduction in crystallite size from 30.91 nm (pure ZnO) to 18.10 nm (6 % Mg doping). SEM images showed uniform morphology with reduced particle agglomeration at optimal doping levels, while FTIR analysis identified characteristic Zn-O and Mg-O bonding vibrations, confirming structural integrity. UV–Vis spectroscopy revealed strong absorbance in the UV region, with the band gap energy decreasing from 3.68 eV (pure ZnO) to 3.16 eV (6 % Mg doping), indicating enhanced optical properties conducive to improved photocatalytic performance. The photocatalytic activity of Mg-doped ZnO nanoparticles was evaluated by degrading Basic Fuchsin (BF) dye under UV light irradiation. The Mg-doped ZnO nanoparticles exhibited significantly enhanced photocatalytic performance compared to undoped ZnO, achieving a maximum degradation efficiency of 99.38 % at 6 % Mg doping within 100 min. Optimal photocatalytic conditions were observed at pH 6, using 0.1 g of catalyst and an initial dye concentration of 10 ppm. These enhancements were attributed to improved electron-hole pair separation and increased generation of reactive oxygen species (ROS), facilitated by the strategic incorporation of Mg. To complement the experimental findings, Density Functional Theory (DFT) simulations were performed, integrating the Conductor-like Screening Model for Realistic Solvation (COSMO-RS), Reduced Density Gradient (RDG), and Quantum Theory of Atoms in Molecules (QTAIM). The DFT analysis revealed enhanced charge

* Corresponding author at: Department of Matter Sciences, Faculty of Science and Technology, University Mohamed Cherif Messaadia of Souk Ahras, 41000, Algeria.
** Corresponding author.
*E-mail addresses:* said.boukerche@univ-soukahras.dz (S. Boukerche), yacinebenguerba@univ-setif.dz (Y. Benguerba).

https://doi.org/10.1016/j.inoche.2025.114274
Received 26 December 2024; Received in revised form 1 March 2025; Accepted 3 March 2025
Available online 8 March 2025

separation, optimized electron transfer dynamics, and stronger adsorption interactions at Mg-doped sites, which promoted efficient ROS generation. The calculated valence band (VB) and conduction band (CB) edge potentials supported the formation of a Z-scheme heterojunction mechanism, enhancing charge separation and minimizing recombination. These theoretical insights aligned with the experimental observations, confirming that Mg doping effectively enhances photocatalytic efficiency by optimizing electronic interactions and promoting reactive surface dynamics. This integrated experimental and theoretical investigation demonstrates that Mg-doped ZnO nanoparticles exhibit superior photocatalytic properties, making them highly effective for environmental remediation applications, particularly in degrading organic pollutants in wastewater treatment. The study highlights the potential of Mg-doped ZnO as a promising photocatalyst for sustainable environmental solutions.

## 1. Introduction

The rapid industrial growth worldwide has led to significant environmental challenges, mainly due to the increasing presence of organic pollutants in water sources [1,2]. Industries such as food processing, leather manufacturing, and textiles are major contributors to releasing synthetic organic pollutants into the environment [3–6]. The adverse effects of these pollutants on human health and ecosystems are well-documented, prompting a global effort to develop practical solutions for their removal [7,8].

Zinc oxide (ZnO) nanostructures have attracted considerable attention over the past few decades due to their versatility in various applications, particularly in photocatalysis. ZnO possesses a unique combination of optical and electrical properties, making it valuable in multiple fields, including photonic sensors [9], photovoltaics [10], light-emitting diodes [11], transparent thin-film transistors [12], and wearable electronics [13,14]. Additionally, ZnO nanostructures have been extensively studied in heterojunction devices with materials such as CuO and silicon, offering promising applications in photodetection [15], gas sensing [16–19], and photoelectrochemical hydrogen production [20]. ZnO's exceptional optical and electrical properties, including high optical transmittance exceeding 80 %, make it a valuable material for optoelectronic devices [21].

As a direct bandgap n-type semiconductor with a bandgap of approximately 3.37 eV and an exciton binding energy of 60 meV [21–24], ZnO has demonstrated its utility in many applications. Its structural compatibility with gallium nitride (GaN) [25] and intense ultraviolet (UV) laser emission make it a promising candidate for laser technologies. ZnO adopts a wurtzite hexagonal crystal structure, with lattice parameters a = 3.25 Å and c = 5.2 Å, contributing to its excellent mechanical and chemical properties [26,27]. Notably, doping ZnO with various metallic ions—such as aluminum [28], indium [29], tin [30], cadmium [31], and magnesium [32]—can significantly modify its electrical and optical characteristics, allowing for tailored performance in specific applications.

ZnO's ability to absorb UV light while remaining transparent in the visible spectrum makes it an ideal material for UV sensors, while its piezoelectric and pyroelectric properties further expand its applicability [33]. Moreover, ZnO's environmental safety—especially in comparison to materials like GaN, BN, SiC, ZnS, and CdS—has increased interest in its use in eco-friendly devices [34,35]. Its biocompatibility also opens up potential applications in medical devices, where using safe and non-toxic materials is crucial [33].

Doping plays a crucial role in tuning ZnO's optoelectronic properties. As Asadi et al. [36] and Okeke et al. [37] reported that native defects such as vacancies, interstitials, and morphological changes significantly influence ZnO's optical and electrical characteristics. Understanding how impurity atoms and defects integrate into ZnO's crystal structure is essential for controlling its bandgap, emission properties, and conductivity. Magnesium (Mg) doping, in particular, has gained attention due to its ability to increase ZnO's bandgap by incorporating $Mg2^{+}$ ions, which have a similar ionic radius to $Zn2^{+}$ (0.66 Å for $Mg2^{+}$ compared to 0.74 Å for $Zn2^{+}$) [38–42]. This similarity makes Mg an ideal dopant, enhancing ZnO's optical and electronic properties without significantly disrupting the crystal lattice.

Recent studies have demonstrated that Mg-doped ZnO nanoparticles exhibit significant improvements in photocatalytic performance. For instance, Mg-doped ZnO nanostructures have shown a 200 % increase in methylene blue degradation efficiency under sunlight compared to pure ZnO [43]. Similarly, Wang et al. [44] reported that Mg-doped ZnO synthesized via an auto-combustion method achieved 80 % dye degradation, whereas pure ZnO exhibited only 30 % efficiency. Furthermore, Ievtushenko et al. [45] investigated the degradation efficiency of methyl orange (MO) dye using Mg-doped ZnO nanostructures deposited by atmospheric pressure MOCVD. Their results showed 100 % dye degradation with ZnO-Mg (2.4 at. %) after 9 h, compared to only 22 % efficiency for pure ZnO. These findings highlight the potential of Mg doping to enhance photocatalytic activity significantly. Other studies have also reported substantial improvements in the degradation of organic dyes, including Rhodamine B (RhB), with Mg doping, leading to higher degradation rates and kinetic constants [46,47].

Despite the substantial progress in ZnO photocatalysis, challenges remain in fully understanding and optimizing its degradation efficiency for practical applications. While Mg doping is known to enhance the photocatalytic activity of ZnO, detailed studies on its effects under varying experimental conditions—such as different doping concentrations, catalyst mass, pH, initial pollutant concentration, and temperature—are still limited. Furthermore, a comprehensive theoretical understanding of the interaction between Mg-doped ZnO and organic pollutants is essential for rationally designing efficient photocatalysts.

While the photocatalytic properties of Mg-doped ZnO have been investigated in previous years, less has been determined about how different Mg doping concentrations and reaction parameters affect the degradation efficiency of pollutants such as Basic Fuchsin (BF) dye. The photocatalytic degradation of BF dye using Mg-doped ZnO nanoparticles has not yet been examined. Furthermore, few thorough theoretical models support experimental results. This work fills these gaps by methodically analyzing the photocatalytic degradation of BF dye under UV light using Mg-doped ZnO nanoparticles synthesized with varying Mg concentrations. The novelty of this work results from its comprehensive integration of experimental and computational approaches, which together provide new insights into the underlying mechanisms of photocatalysis, allowing for a better understanding of the interactions that drive degradation efficiency in Mg-doped ZnO systems.

The novelty of this work lies in its comprehensive integration of experimental and computational approaches, providing new insights into the underlying mechanisms of photocatalysis and enabling a deeper understanding of the interactions that drive degradation efficiency in Mg-doped ZnO systems. This study uses various analytical techniques to synthesize and characterize Mg-doped ZnO nanoparticles to investigate their structural, morphological, and optical properties. X-ray diffraction (XRD) examines the crystalline structure while scanning electron microscopy (SEM) assesses nanoparticle morphology. Fourier transform infrared spectroscopy (FTIR) provides insights into surface chemistry and bonding interactions, and UV–Visible spectroscopy evaluates the optical properties of the synthesized nanoparticles. Photocatalytic degradation of Basic Fuchsin dye under UV light was systematically analyzed, focusing on the effects of Mg doping concentration,

photocatalyst mass, solution pH, dye concentration, and reaction temperature. A kinetic model was developed to describe the degradation process using pseudo-first-order kinetics. To complement the experimental findings, Density Functional Theory (DFT) simulations were conducted, including a Conductor-like Screening Model for Realistic Solvation (COSMO-RS) for charge distribution, Reduced Density Gradient (RDG) analysis for non-covalent interactions, and Quantum Theory of Atoms in Molecules (QTAIM) for bond critical points. This integrated experimental and theoretical approach offers a comprehensive understanding of the photocatalytic behavior of Mg-doped ZnO nanoparticles, contributing to developing highly efficient materials for environmental remediation applications.

## 2. Materials and methods

### 2.1. Materials

The materials and chemicals used in this study were all analytical grade, acquired from Sigma Aldrich. The precursor for zinc oxide was zinc nitrate tetrahydrate (($Zn(NO_3)_2$, $4H_2O$, 99.0 %). The solvent was distilled water. NaOH (sodium hydroxide) solution was used to maintain pH. The manganese precursor for doped nanoparticles was magnesium chloride hexahydrate ($MgCl_2$, $6H_2O$, 99.0 %). Ethanol and deionized water were used for washing.

### 2.2. Synthesis of Mg-doped ZnO nanoparticles

Mg-doped ZnO nanoparticles were synthesized using a standard co-precipitation method to ensure uniform doping and high crystallinity. Initially, zinc nitrate tetrahydrate ($Zn(NO_3)_2{\cdot}4H_2O$, 99.0 %) was dissolved in deionized water to prepare a 0.5 M solution. The mixture was stirred at 80 °C for one hour using a magnetic stirrer to ensure complete dissolution and homogeneity. Simultaneously, a 0.5 M NaOH solution was prepared in 500 mL of deionized water. The NaOH solution was then added dropwise to the zinc nitrate solution under constant stirring at 80 °C, maintaining the reaction conditions necessary for the co-precipitation process. The reaction mixture was subjected to sonication for 20 min after NaOH was added entirely to enhance the nucleation and growth of ZnO nanoparticles. The precipitates formed were allowed to age at room temperature for 6 h to ensure the complete growth of ZnO crystals. The resulting nanoparticles were collected by centrifugation at 4000 rpm for 20 min, followed by thorough washing with ethanol and deionized water to remove residual ions or impurities. The washed precipitates were dried in a hot air oven at 100 °C for 24 h. Subsequently, the dried powders were calcined at 500 °C for one hour to enhance crystallinity and eliminate any remaining organic residues [48]. The same procedure was followed to synthesize Mg-doped ZnO nanoparticles, adding magnesium chloride ($MgCl_2{\cdot}6H_2O$) as the doping precursor. The required stoichiometric amounts of magnesium chloride were added to the zinc nitrate solution to achieve Mg doping concentrations of 2 %, 4 %, 6 %, and 8 %, corresponding to 0.16 g, 0.36 g, 0.58 g, and 0.84 g of $MgCl_2{\cdot}6H_2O$, respectively. The Mg-doped ZnO nanoparticles were designated as 2 % Mg-doped ZnO, 4 % Mg-doped ZnO, 6 % Mg-doped ZnO, and 8 % Mg-doped ZnO. An identical synthesis method was employed for preparing pure ZnO nanoparticles, ensuring consistent experimental conditions [49]. This controlled doping method ensures the uniform incorporation of $Mg^{2+}$ ions into the ZnO lattice, influencing the structural and optical properties of the nanoparticles. The consistency in the synthesis conditions and precise stoichiometric control contributed to the reproducibility and reliability of the Mg-doped ZnO samples.

### 2.3. Photocatalytic activity

The photocatalytic treatment of wastewater was carried out in a photoreactor using a UV–visible lamp that produced light with a 25 W intensity. The basic fuchsin degradation process was examined to assess the generated nanoparticles' catalytic efficacy. The fundamental process of removing basic fuchsin was monitored over time. Double-distilled water creates a dye solution with 10 parts per million (ppm) concentration. To assess the effect of adsorption during the first half-hour, an equilibrium condition is reached by mixing 100 ml of dye solution made from each sample with 10 mg of photocatalyst. At the same time, the mixture is dark for half an hour. Every sample is subjected to a UV–visible spectroscopic study every 30 min.

The following formula can be used to calculate the percentage of degradation, decolorization, or removal [50]:

$$Degradationefficiency = \frac{C_O - C}{C_O} \times 100 \quad (1)$$

C0 represents the initial dye solution concentration, and C represents the final dye solution concentration in time.

### 2.4. Characterizations

Several methods were used to examine the impact of Mg-doped ZnO on the nanoscale structure, shape, and spectral properties of Mg-doped ZnO. Mg-doped ZnO NPs were analyzed chemically and elementally morphology using SEM. XRD was used to analyze the structure, Rigaku Ultima IV diffractometer equipped with Cu-Kα radiation (λ = 1.5418Å). SEM was utilized to investigate the surface morphologies of ZnO NPs doped with magnesium using FEI QUANTA 250. Fourier transformer infrared spectroscopy, or FTIR, investigated functional groups and determined a material's molecular structure. The optical absorption spectra of Mg-doped ZnO nanoparticles were analyzed using a Shimadzu UV– vis 3600 plus spectrophotometer in UV–Vis–NIR spectral region (200–800) nm. The optical and electrical properties of synthesized pure and Mg-doped ZnO NPs were investigated using UV–visible spectroscopy and a photoluminescence spectrometer (photoLab 6600-UV–VIS).

### 2.5. Computational methodology

A series of theoretical simulations were conducted to correlate the quantum chemical properties of Mg-doped ZnO NPs with their experimentally measured photocatalytic degradation efficiencies. The DFT framework, explicitly employing the B3LYP functional [51–55], was utilized through the Turbomole 7.4 software package [52,56–60]. The def-SV(P) basis set [51,53,61–63] was chosen for its ability to accurately model the electronic structure of ZnO and Mg-doped ZnO systems, while the M06-2X functional [19,64–67] was employed to account for dispersion interactions and long-range electron correlation effects, essential for studying the photocatalytic mechanisms in nanostructures.

Conductor-like Screening Model for Realistic Solvation (COSMO-RS) calculations were performed to refine our understanding of the photocatalytic behavior further. These provided insights into the charge distribution across the Mg-doped ZnO cluster, allowing us to predict reactive sites and assess the system's reactivity during photocatalytic degradation.

A comprehensive examination of NCI within the Mg-doped ZnO@BF dye system was conducted using the (RDG method [68,69] and QTAIM [70–72]. This approach identified and characterised weak interactions such as hydrogen bonding, van der Waals forces, and steric repulsions, which are critical to understanding organic pollutants' adsorption and degradation processes on the catalyst surface. The RDG analysis, carried out using the Multiwfn program [73], visualized these interactions based on electron density (ρ) and its gradients, providing a detailed map of interaction strength [74–76]. This analysis is vital for elucidating the stabilization mechanisms of BF dye molecules on Mg-doped ZnO NPs and the efficient charge transfer that drives photocatalysis.

Color-coded scatter plots were also constructed using gnuplot [77] to illustrate the interaction profiles between the dye molecules and the

photocatalyst. QTAIM provided a quantitative assessment of bonding interactions within the system by analyzing key topological parameters at Bond Critical Points (BCPs), offering a deeper understanding of the interactions that influence the photocatalytic degradation process. The spatial arrangement and molecular interaction network were visualized using the VMD interface [78], clearly presenting how Mg doping influences electron distribution and interaction sites within the ZnO cluster.

## 3. Results and discussion

### 3.1. Structural characterization by X-ray diffraction (XRD)

XRD is a critical technique for assessing nanomaterials' crystalline structure, phase purity, and crystallite size. This study employed XRD to investigate the structural properties of pure and Mg-doped ZnO nanoparticles synthesized via a co-precipitation method. The data obtained from XRD confirms the successful doping of Mg into the ZnO lattice and provides essential information on the crystallinity and phase stability of the synthesized materials. As shown in Fig. 1 (a), the XRD patterns for pure ZnO exhibit characteristic diffraction peaks at 2θ = 31.84°, 34.52°, and 36.36°, corresponding to the (1 0 0), (0 0 2), and (1 0 1) planes of the hexagonal wurtzite structure of ZnO, consistent with JCPDS file No. 36-1451 [79]. These sharp and intense peaks indicate high crystallinity in the ZnO nanoparticles. Additional diffraction peaks at 2θ = 45.54°, 47.64°, 56.70°, 58.32°, 62.96°, 66.34°, and 75.38° are observed, corresponding to the (4 2 2), (1 0 2), (2–10), (4 2 2), (1 0 3), (2 0 0), and (2 0 2) planes, further confirming the structural integrity of the wurtzite phase.

Upon doping with Mg, notable changes are observed in the diffraction patterns, particularly a shift in the positions of the prominent peaks, as shown in Fig. 1 (b). This shift is most distinguished for the (1 0 0) and (0 0 2) planes. The slight change towards higher 2θ values can be attributed to successfully incorporating $Mg^{2+}$ into the ZnO lattice, replacing $Zn^{2+}$ ions. Given that $Mg^{2+}$ has a smaller ionic radius (0.66 Å) compared to $Zn^{2+}$ (0.74 Å), the substitution leads to lattice contraction, which is reflected in the peak shift [40–42]. This observation confirms that Mg has been successfully doped into the ZnO matrix, resulting in a minor alteration of the lattice parameters while maintaining the hexagonal wurtzite structure. The absence of additional peaks or new phases in the XRD patterns of Mg-doped ZnO nanoparticles suggests that the doping process did not introduce secondary phases, such as MgO, and that $Mg^{2+}$ is homogeneously distributed within the ZnO lattice [80]. The high purity of the phase is critical, as the presence of secondary phases could hinder photocatalytic performance by acting as recombination centers for photo-generated charge carriers [81–83].

Furthermore, the XRD data were used to calculate the crystallite sizes of the nanoparticles using Scherrer's equation [84]:

$$D = \frac{K.\lambda}{\beta.cos\theta} \quad (2)$$

where D is the average crystallite size, K is the shape factor (typically 0.9), λ is the X-ray wavelength (0.15406 nm for Cu Kα radiation), β is the full-width at half-maximum (FWHM) of the diffraction peak, and θ is the diffraction angle. The results, summarized in Table 1, indicate a progressive decrease in crystallite size with increasing Mg doping. Specifically, the crystallite size decreases from 30.91 nm for pure ZnO to 26.52 nm, 23.68 nm, 18.10 nm, and 24.11 nm for Mg-doped ZnO samples with 2 %, 4 %, 6 %, and 8 % Mg, respectively.

The reduction in crystallite size with increasing Mg concentration is attributed to the smaller ionic radius of $Mg2^{+}$, which leads to lattice shrinkage and reduced particle size. Similar trends have been observed in other studies involving transition metal doping in ZnO, where the dopant ion's size influences the crystallite dimensions [85].

Interestingly, a slight increase in crystallite size was observed at 8 % Mg doping compared to the 6 % sample, which may be attributed to agglomeration or slight lattice distortions at higher dopant concentrations. This behavior is commonly reported in the literature when doping concentrations exceed an optimal limit, leading to strain relaxation or particle coalescence during synthesis [42,80,81]. Thus, while Mg doping reduces the crystallite size, higher doping levels may introduce competing effects, such as lattice distortion and defect formation, which could affect the material's photocatalytic efficiency.

In terms of structural implications, the reduction in crystallite size with Mg doping is beneficial for photocatalysis. Smaller crystallite sizes result in larger surface areas, which enhance the interaction between the catalyst and the target molecules, such as dyes or pollutants in water

**Table 1**
Crystallite size (nm) of all synthesized pure and Mg-doped ZnO NPs.

| Sample | Crystalline size (nm) |
|---|---|
| Pure ZnO NPs | 30.91 |
| Mg-doped 2 % | 26.52 |
| Mg-doped 4 % | 23.68 |
| Mg-doped 6 % | 18.10 |
| Mg-doped 8 % | 24.11 |

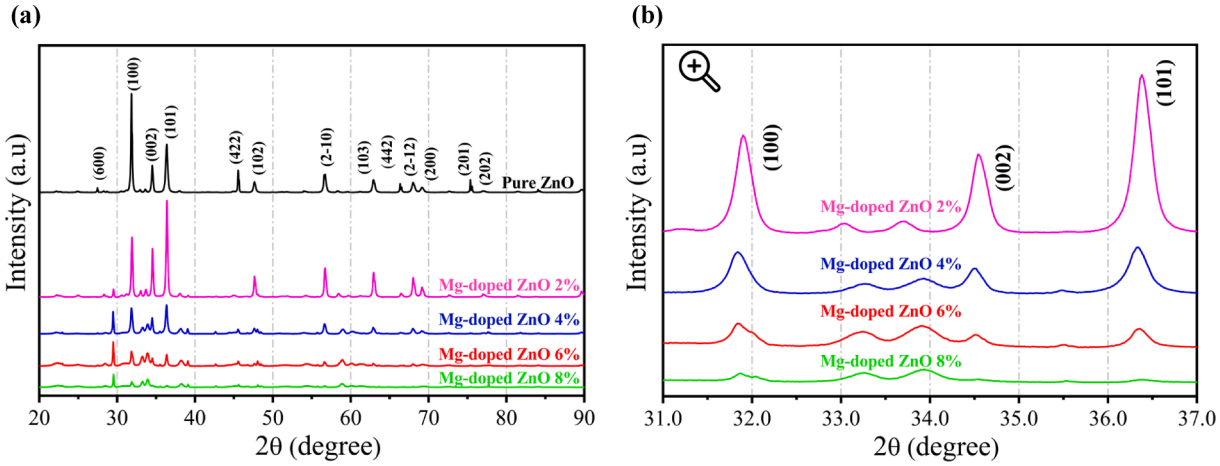


**Fig. 1.** XRD patterns of pure and Mg-doped ZnO NPs synthesized by the co-precipitation method and annealed at 500 °C for 1 h: (a) wide-angle XRD patterns illustrating phase purity across all Mg doping concentrations, and (b) magnified view of the (1 0 0), (0 0 2), and (1 0 1) peaks, highlighting the shift in peak positions as Mg content increases.

treatment applications [86]. Moreover, the slight shifts in the XRD peaks suggest that Mg incorporation could also influence the electronic properties of ZnO, potentially altering its bandgap and charge carrier dynamics, which are critical for improving photocatalytic efficiency under UV or visible light irradiation.

Therefore, the XRD results confirm that Mg doping significantly alters the structural properties of ZnO NPs. These changes are expected to influence their photocatalytic performance, which will be further explored in subsequent sections on photocatalytic degradation. The phase purity, crystallinity, and controlled reduction in crystallite size all point to the successful synthesis of Mg-doped ZnO nanoparticles with enhanced potential for environmental applications, such as the

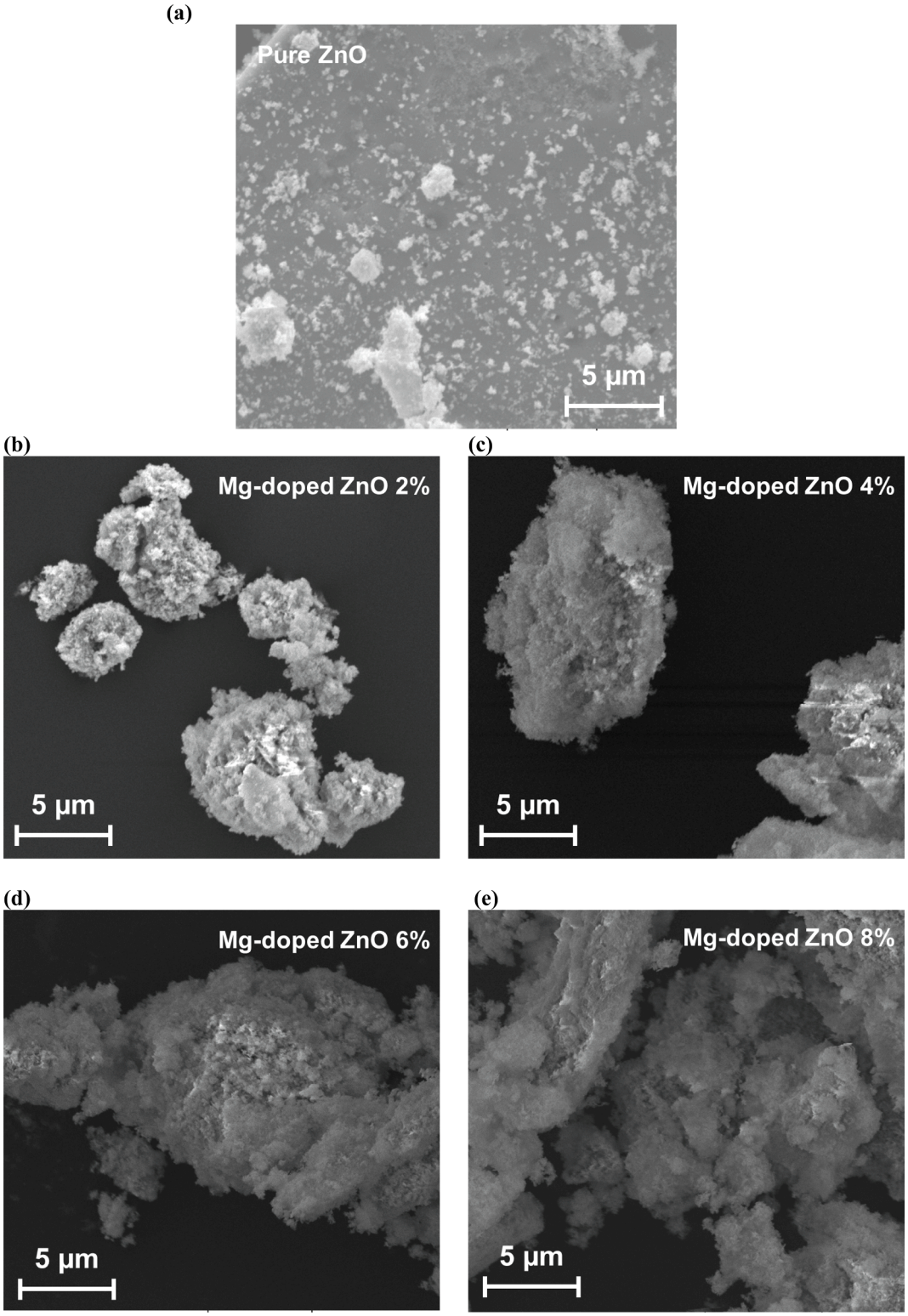


**Fig. 2.** SEM images of pure and Mg-doped ZnO NPs at 5-µm magnification and varying Mg doping concentrations: (a) pure ZnO, (b) 2% Mg-doped ZnO, (c) 4% Mg-doped ZnO, (d) 6% Mg-doped ZnO, and (e) 8% Mg-doped ZnO, showing changes in particle agglomeration and morphology with increasing Mg content.

degradation of organic pollutants.

### 3.2. Morphological observations by SEM

SEM was employed to investigate the surface morphology and particle size distribution of pure ZnO and Mg-doped ZnO NPs. The SEM images, as shown in Fig. 2, provide clear evidence of how Mg doping influences the morphology and aggregation behavior of the nanoparticles. These observations are critical, as nanoparticle morphology plays a key role in determining the material's surface area, charge transfer efficiency, and photocatalytic performance. Fig. 2 (a) depicts the SEM image of pure ZnO NPs, which exhibit a relatively uniform distribution of small, spherical agglomerates. The pure ZnO particles are tightly packed, and their aggregation is typical of nanoparticles synthesized via co-precipitation. These particles tend to cluster due to their high surface energy, which encourages the formation of agglomerates during drying and annealing processes [87]. Upon doping with Mg, the morphology of the ZnO nanoparticles undergoes significant changes, as illustrated in Fig. 2 (b–e). The nanoparticles remain agglomerated at 2 % Mg doping (Fig. 2 (b)), but the clusters appear more loosely packed than pure ZnO. This may indicate that $Mg^{2+}$ ions, upon substitution into the ZnO lattice, disrupt the regular crystallization process, resulting in a less compact structure. The introduction of $Mg^{2+}$ likely influences nucleation and growth mechanisms, leading to slight variations in the particle size distribution [88–90].

As the Mg concentration increases to 4 % and 6 % (Fig. 2 (c) and (d)), a noticeable increase in particle agglomeration is observed. The NPs form larger, more compact clusters than pure ZnO and the 2 % Mg-doped samples. This increased agglomeration can be attributed to enhanced lattice strain caused by the incorporation of $Mg^{2+}$ ions, where the substitution of $Mg^{2+}$ for $Zn^{2+}$ within the ZnO lattice likely leads to a contraction of the lattice, promoting particle aggregation as the system tries to minimize surface energy [87]. The higher Mg doping levels may also induce more significant changes in surface charge distribution, altering the inter-particle forces and resulting in more substantial agglomeration [37,91]. At 8 % Mg doping (Fig. 2 (e)), the SEM images reveal the formation of even larger and more irregular aggregates. These structures are composed of a highly clustered morphology, with particles forming dense, uneven agglomerates. The pronounced agglomeration at this doping level may be due to the saturation of $Mg^{2+}$ in the ZnO lattice, causing increased lattice distortion and defect formation, such as oxygen vacancies, which could enhance particle interaction and aggregation [37,87]. This behavior is characteristic of doped nanomaterials, where exceeding a critical doping concentration threshold prevents the effective incorporation of excess dopant ions into the lattice, ultimately leading to particle coalescence [92]. Interestingly, the SEM images of Mg-doped ZnO nanoparticles also show signs of a rod-like morphology, particularly at higher doping levels. These rod-like structures may be formed due to preferential growth along specific crystallographic directions, which the presence of $Mg^{2+}$ ions can influence. Metal ion doping, including Mg, has been reported to impact the anisotropic growth of ZnO nanoparticles, leading to the development of 1D nanostructures such as nanorods and nanowires. Although not dominant, these morphological features could play a significant role in the photocatalytic performance of the material by enhancing light absorption and charge separation efficiency [88]. The changes in morphology observed in the SEM images directly correlate with the structural modifications introduced by Mg doping. The increased agglomeration and formation of irregular structures with higher Mg content can be attributed to the strain induced within the ZnO lattice and the generation of defects, such as oxygen vacancies, which are known to influence particle interaction and aggregation [93]. These morphological changes are expected to substantially impact the material's photocatalytic properties, as the surface area, defect density, and particle dispersion are critical factors affecting photocatalytic activity. Accordingly, the SEM analysis reveals that Mg doping significantly alters the morphology of ZnO nanoparticles, leading to increased agglomeration and the formation of more compact and irregular structures at higher doping levels. These morphological changes are likely to influence the photocatalytic efficiency of Mg-doped ZnO, as they affect both the surface area and the ability of the material to interact with light and generate reactive species. Further investigation into the specific impact of these morphological features on photocatalytic performance would provide deeper insights into optimizing Mg-doped ZnO for environmental remediation applications.

### 3.3. Analysis of FTIR spectra

FTIR spectroscopy is vital for identifying nanomaterials' functional groups, chemical bonds, and molecular interactions. It provides critical insights into synthesized nanoparticles' surface chemistry and bonding environment, essential for understanding their structural integrity and potential photocatalytic behavior. FTIR is particularly valuable in the context of metal oxide nanoparticles, such as ZnO, as it allows for detecting surface hydroxyl groups, metal–oxygen bonds, and residual organic compounds, all of which can impact the material's properties. Fig. 3 presents the FTIR spectra of pure and Mg-doped ZnO nanoparticles at different doping concentrations (2 %, 4 %, 6 %, and 8 % Mg). The spectral analysis reveals several characteristic peaks corresponding to various functional groups, with significant features identified in the ranges of 3000–3700 $cm^{-1}$, 1300–1400 $cm^{-1}$, and 500–600 $cm^{-1}$. These peaks provide critical information about the chemical composition and structural changes Mg doping induces. The broad absorption band between 3000 $cm^{-1}$ and 3700 $cm^{-1}$ is associated with the O–H stretching vibrations. This peak is characteristic of hydroxyl groups, either from surface-adsorbed water molecules or from Zn-OH and Mg-OH bonds on the surface of the nanoparticles [94–97]. These hydroxyl groups are essential, as they play a key role in photocatalytic reactions, where hydroxyl radicals are generated under UV or visible light irradiation to degrade organic pollutants [83,88]. The intensity and breadth of this peak across all samples, including pure ZnO and Mg-doped ZnO, suggest that surface hydroxyl groups are prevalent regardless of doping concentration. However, slight variations in intensity could indicate changes in the amount of surface hydroxyl groups, potentially influenced by the incorporation of $Mg^{2+}$ ions. The peak around 1362 $cm^{-1}$, observed consistently across the spectra, corresponds to the bending vibrations of O–H bonds, further confirming the presence of hydroxyl groups on the nanoparticle surfaces. This peak is crucial for

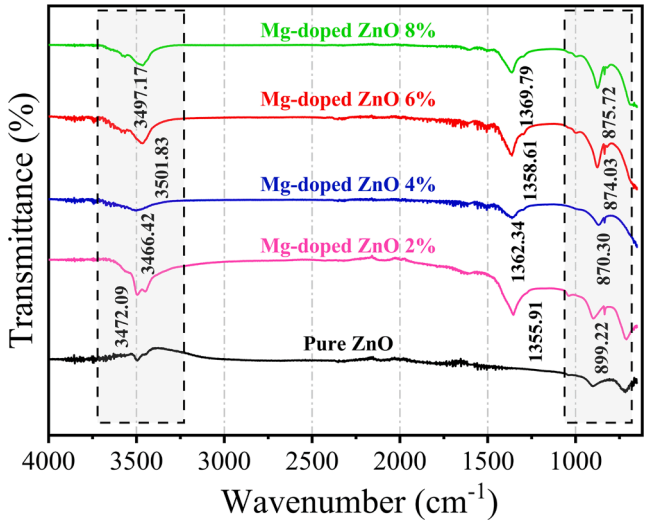


**Fig. 3.** FTIR spectra of pure and Mg-doped ZnO nanoparticles at varying Mg doping concentrations (2%, 4%, 6%, and 8%), showing characteristic O–H, Zn–O, Mg–O, and C–H bond vibrations and their shifts due to Mg incorporation.

understanding the surface reactivity of the nanoparticles, as the density of surface hydroxyl groups can directly impact their photocatalytic efficiency [98]. Notably, this peak's persistence with increasing Mg doping suggests that the doping process does not significantly disrupt the surface hydroxyl bonding. However, slight shifts and intensity changes imply some modification in surface chemistry. In the low wavenumber region, between 500 cm$^{-}$1 and 600 cm$^{-}$1, the spectra exhibit prominent peaks corresponding to the stretching vibrations of Zn-O bonds, a signature feature of the wurtzite ZnO structure [83]. These peaks are present in both pure and Mg-doped samples, confirming that the fundamental crystal structure of ZnO remains intact after Mg doping. However, as Mg concentration increases, a slight shift in the position of the Zn-O stretching peaks is observed. This shift indicates that $Mg^{2+}$ ions have successfully substituted for $Zn^{2+}$ within the ZnO lattice. This structural change is a key confirmation of the successful incorporation of Mg into the ZnO lattice, further supported by the absence of secondary phases or additional peaks that would indicate the formation of MgO or other impurities [82,99].

The emergence of a peak around 876 cm$^{-1}$ can be attributed to C–H bending vibrations, likely originating from residual organic compounds such as alcohols or stabilizers used during the synthesis process. The presence of this peak, particularly in the Mg-doped samples, suggests that Mg incorporation may influence the surface chemistry, potentially allowing organic residues to remain adsorbed on the surface of the nanoparticles. Such residues could result from incomplete annealing or the complexation of organic molecules with $Mg^{2+}$ during synthesis [95]. While these organic species are generally undesired, their influence on photocatalytic activity may vary depending on their interaction with surface active sites. Furthermore, in the 1300–1400 cm$^{-1}$ range, we observe peaks associated with the Mg–O bond stretching, particularly prominent in the Mg-doped samples. These peaks increase in intensity with higher Mg doping concentrations, indicating that $Mg2^{+}$ ions are not only incorporated into the ZnO lattice but also interact with oxygen atoms to form Mg-O bonds. These peaks' appearance and the shift in the Zn-O bond vibrations provide strong evidence of successful Mg doping, with no signs of phase separation or the formation of secondary MgO phases [83,94].

Consequently, the FTIR analysis provides strong evidence of successfully incorporating $Mg^{2+}$ ions into the ZnO lattice, with no indications of secondary phases or impurities. The presence of key functional groups such as O–H and the shifts in Zn–O and Mg–O bond vibrations confirm that Mg doping induces subtle yet essential changes in the chemical structure and surface chemistry of ZnO NPs. These structural and chemical modifications, as revealed by FTIR, are expected to influence the photocatalytic properties of the Mg-doped ZnO, mainly through enhanced surface reactivity and altered charge transfer dynamics.

### 3.4. Analysis of optical properties

The optical properties of pure and Mg-doped ZnO NPs were investigated through UV–Vis absorption spectroscopy, as illustrated in Fig. 4. The spectra were recorded over the 200–500 nm wavelength range, providing crucial insights into the synthesized nanoparticles' electronic transitions and absorption behavior. These optical characteristics are essential for evaluating their potential applications in photocatalysis and optoelectronic devices, as they are directly linked to the material's band gap and photo-response efficiency.

The absorption spectrum of pure ZnO nanoparticles exhibits a prominent peak around 370 nm, corresponding to the intrinsic band edge absorption of ZnO, which is characteristic of its wide band gap [88,100,101]. This peak is associated with electronic transitions from valence to conduction bands. With the introduction of Mg as a dopant, significant shifts in the absorption edge and variations in absorption intensity were observed, indicating the impact of Mg incorporation on the optical properties of ZnO.

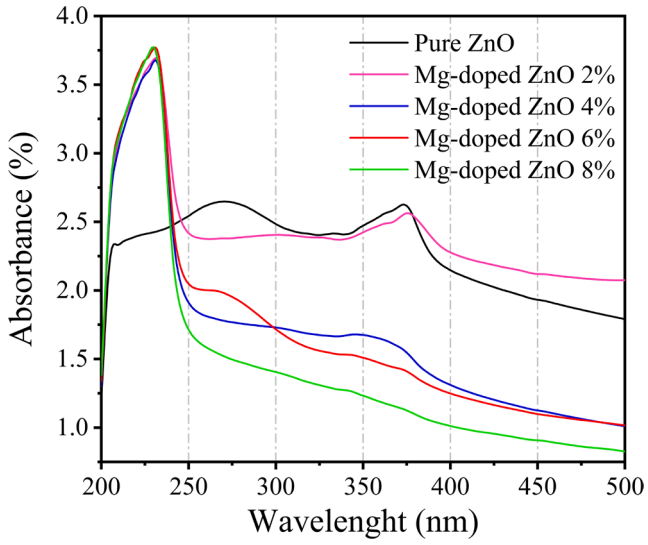


**Fig. 4.** UV–Vis absorption spectra of pure and Mg-doped ZnO NPs with varying Mg concentrations, illustrating shifts in the absorption edge and changes in absorbance intensity.

In detail, the absorption spectrum of pure ZnO shows a sharp excitonic peak at approximately 250 nm, corresponding to the intrinsic band edge transition. This feature is attributed to the excitonic absorption near the band gap of ZnO, which confirms its high crystallinity and defect-free structure. Additionally, a shoulder around 350 nm is observed, which is linked to defect states such as oxygen vacancies and zinc interstitials, contributing to sub-bandgap absorption. These defect-related states are characteristic of ZnO and are known to influence its photocatalytic activity.

Upon doping with 2 % Mg, a slight redshift in the absorption edge is observed, indicating a shift towards longer wavelengths. This redshift suggests a reduction in the band gap due to lattice strain induced by incorporating $Mg^{2+}$ ions into the ZnO lattice, which modifies the electronic band structure [100]. This behavior enhances the absorption of lower-energy photons, improving the photocatalytic potential of Mg-doped ZnO under visible light. The increased absorbance at this doping level can be attributed to enhanced defect density, particularly oxygen vacancies, and changes in particle size and surface morphology, collectively contributing to higher light absorption [102].

However, at higher Mg concentrations (4 %, 6 %, and 8 %), a blue shift in the absorption edge and a noticeable decrease in absorbance intensity are observed. This blue shift is associated with a widening band gap, which is attributed to the Burstein-Moss effect, where increased carrier concentration from Mg doping leads to band filling and a consequent shift to higher energies. Additionally, the reduction in absorbance intensity at higher Mg doping levels can be linked to increased particle agglomeration, which reduces the effective surface area available for light absorption. Moreover, excessive Mg incorporation introduces additional lattice defects, acting as scattering centers and diminishing the overall light absorption efficiency.

The shoulder at ~350 nm diminishes progressively with increasing Mg doping, suggesting reduced defect states such as oxygen vacancies. This observation aligns with the improved crystallinity confirmed by XRD analysis, indicating that Mg doping effectively modifies the defect landscape of ZnO. The overall blue shift in the absorption edge at higher doping levels suggests partial band gap recovery due to the interplay between quantum confinement effects and defect formation within the ZnO lattice [82,88,100,102].

The optical band gap energies ($E_g$) of the pure and Mg-doped ZnO nanoparticles were calculated using the Tauc plot method, derived from UV–Vis absorption data, as shown in Fig. 5. The Tauc plot is constructed using the following equation [103]:

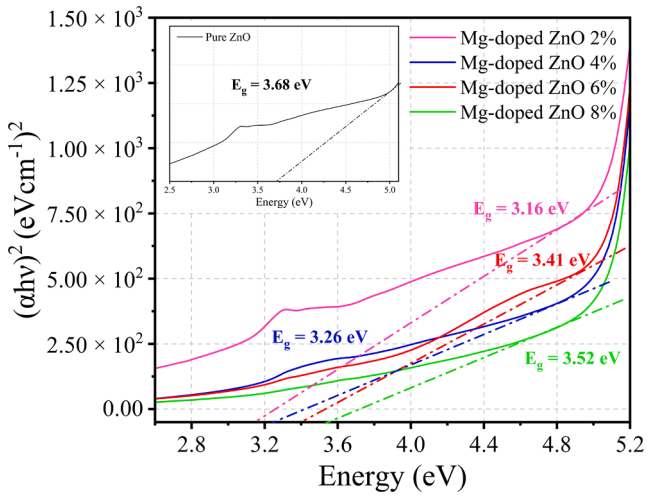


**Fig. 5.** Tauc plots to determine optical band gap energies of pure and Mg-doped ZnO nanoparticles, showing band gap reduction with increasing Mg doping levels.

$$\alpha h\nu = A\left(h\nu - E_g\right)^{1/2} \tag{3}$$

Here, $\alpha$ denotes the absorption coefficient, $h$ is Planck's constant, $\nu$ is the frequency of the incident light, and $A$ is a proportionality constant.

The calculated band gap for pure ZnO was 3.68 eV, which appears to be higher than the typical bulk ZnO band gap of ~3.37 eV. This excessive band gap value can be attributed to the quantum confinement effect resulting from the nanoscale size of the ZnO particles. When the particle size approaches the exciton Bohr radius, quantum confinement causes a widening of the band gap due to the spatial restriction of charge carriers. Additionally, surface effects such as increased surface-to-volume ratio and surface defects, including oxygen vacancies, can contribute to localized energy states, influencing the optical band gap. These factors collectively result in the observed blue shift and the higher band gap value for the undoped ZnO nanoparticles [88,100].

A significant reduction in the band gap is observed upon incorporation of Mg as a dopant. For the 2 % Mg-doped ZnO, the band gap decreased to 3.16 eV, indicating the impact of Mg doping on narrowing the band gap. This reduction is attributed to the substitution of $Zn^{2+}$ with $Mg^{2+}$ in the ZnO lattice, which induces lattice strain due to the smaller ionic radius of $Mg^{2+}$. This lattice distortion alters the electronic band structure, effectively reducing the energy gap between the valence and conduction bands [102,104]. However, the band gap values gradually increase as the Mg doping concentration increases. The band gaps for 4 %, 6 %, and 8 % Mg-doped ZnO were calculated to be 3.26 eV, 3.41 eV, and 3.52 eV, respectively. This trend can be explained by the complex interplay between particle size, quantum confinement effects, and defect density [103]. At higher doping concentrations, particle agglomeration may occur, leading to an increase in the effective particle size, which reduces the quantum confinement effect, thereby causing a slight widening of the band gap.

Additionally, excessive Mg incorporation can introduce more significant defect formation, such as oxygen vacancies and interstitial defects, which can act as scattering centers, altering the material's electronic properties. These defects contribute to localized energy levels within the band gap, influencing the absorption characteristics and leading to the observed blue-shift in the absorption edge and a partial recovery of the band gap energy [93,102]. The ability to tune the band gap through controlled Mg doping has significant implications for the photocatalytic and optoelectronic applications of ZnO nanoparticles. The redshift in the absorption edge and band gap reduction at lower doping concentrations enhances the material's ability to absorb visible light, improving photocatalytic efficiency. Conversely, the increased band gap at higher Mg concentrations benefits applications requiring higher energy photon absorption, such as UV sensors and optoelectronic devices [91,104].

Consequently, the systematic modulation of the optical properties of ZnO through Mg doping demonstrates the potential of these nanoparticles for a range of applications, including photocatalysis, UV detection, and optoelectronic devices. This study provides a comprehensive understanding of how Mg doping influences the electronic structure and optical behavior of ZnO nanoparticles.

### 3.5. Photocatalytic analysis

The photocatalytic degradation of BF dye was systematically investigated using pure ZnO and Mg-doped ZnO nanoparticles under UV light irradiation to assess their photocatalytic efficiencies. The calibration curve for BF dye concentrations, presented in Fig. 6 (a), exhibits a highly linear relationship between absorbance and dye concentration, with an $R^2$ value exceeding 0.99. This strong linearity confirms the accuracy and precision of the absorbance measurements, validating the robustness of the analytical system developed for monitoring the photocatalytic degradation process. Such validation is essential for ensuring the reproducibility and reliability of the experimental results, which is critical in photocatalytic degradation studies.

Photocatalytic performance was evaluated by tracking the reduction in BF dye concentration over time, with degradation efficiencies calculated for pure and Mg-doped ZnO samples under varying experimental conditions. These conditions included changes in Mg doping concentration, photocatalyst mass, solution pH, initial dye concentration, and reaction temperature, as illustrated in Figs. 6 and 7. This comprehensive investigation provides valuable insights into the critical parameters influencing the photocatalytic activity of the synthesized ZnO-based materials.

To further elucidate the photocatalytic degradation mechanism, kinetic analysis was conducted by plotting $\ln(C_0/C)$ versus time, where $C_0$ and $C$ represent the initial and instantaneous dye concentrations, respectively. This approach enabled the determination of reaction rate constants ($k$) under various experimental conditions. The high linearity observed in the kinetic plots, supported by strong $R^2$ values, indicates that the degradation process adheres to pseudo-first-order reaction kinetics across all tested scenarios. The kinetics of the degradation process were modeled using the pseudo-first-order equation [102]:

$$ln\frac{C_0}{C} = kt \tag{4}$$

where $k$ represents the reaction rate constant, and $t$ is the reaction time.

This extensive analysis thoroughly explains the key factors affecting the photocatalytic degradation of BF dye by ZnO and Mg-doped ZnO NPs. The results demonstrate that Mg doping significantly enhances the photocatalytic efficiency of ZnO, with optimal degradation observed under specific conditions of catalyst mass, solution pH, and dye concentration. Furthermore, the kinetic data affirm the suitability of the pseudo-first-order model in describing the photocatalytic degradation process. These findings highlight the potential of Mg-doped ZnO NPs for effective environmental remediation, particularly in the degradation of organic pollutants.

#### 3.5.1. Effect of Mg doping on photocatalytic degradation of BF dye

The photocatalytic performance of ZnO NPs, modified by Mg doping, was evaluated for the degradation of BF dye. Fig. 6 (b) illustrates the impact of varying Mg doping percentages on degradation efficiency. Mg-doped ZnO acts as a photocatalyst by generating electron-hole pairs upon UV light irradiation. These electron-hole pairs lead to the formation of ROS, such as hydroxyl (•OH) and superoxide radicals ($\bullet O_2^-$), both of which are essential for breaking down organic pollutants like BF dye [105]. Upon UV light exposure, electrons in the valence band are excited

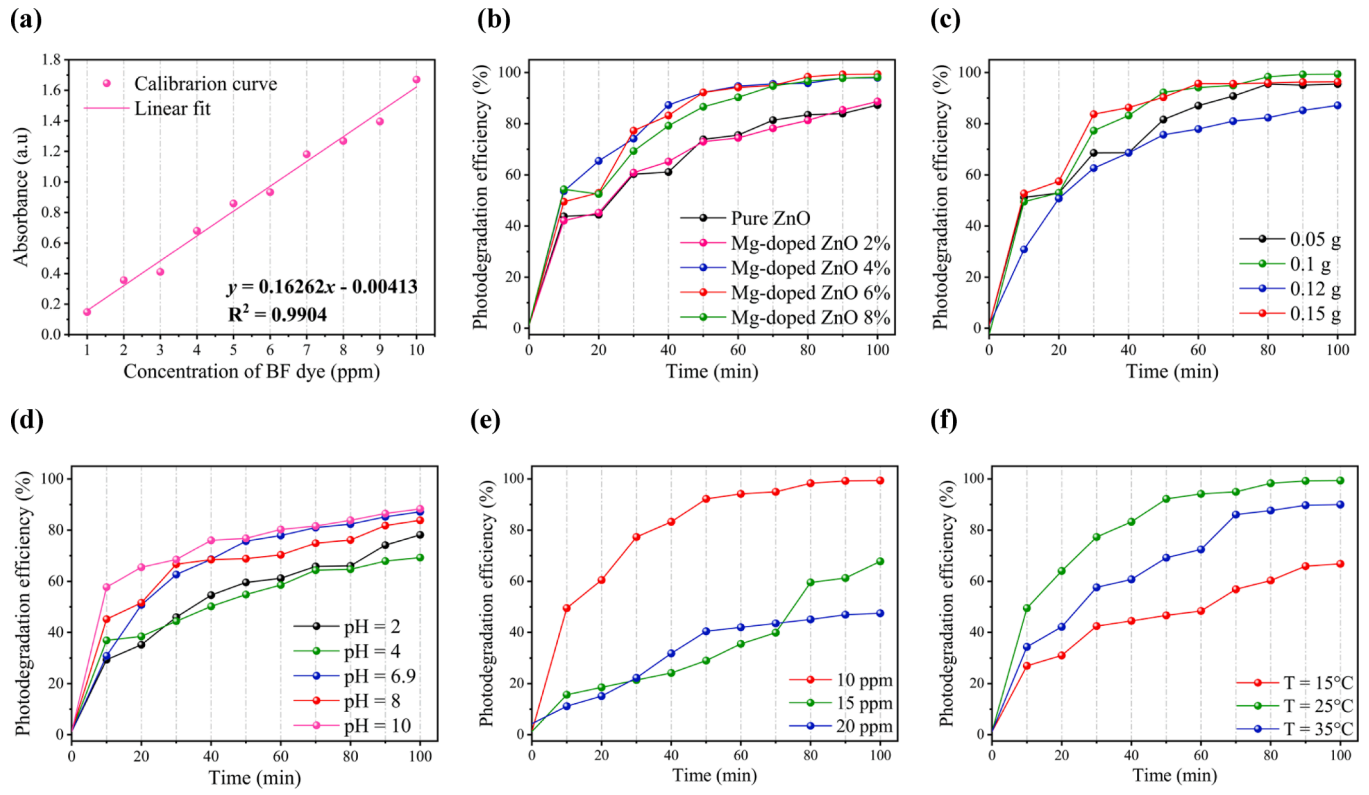


**Fig. 6.** Photocatalytic degradation efficiency of BF dye using pure and Mg-doped ZnO NPs under varying experimental conditions: (a) Calibration curve of BF dye concentration; (b) Effect of Mg doping percentage; (c) Effect of photocatalyst mass; (d) Effect of initial solution pH; (e) Effect of initial dye concentration; and (f) Effect of reaction temperature.

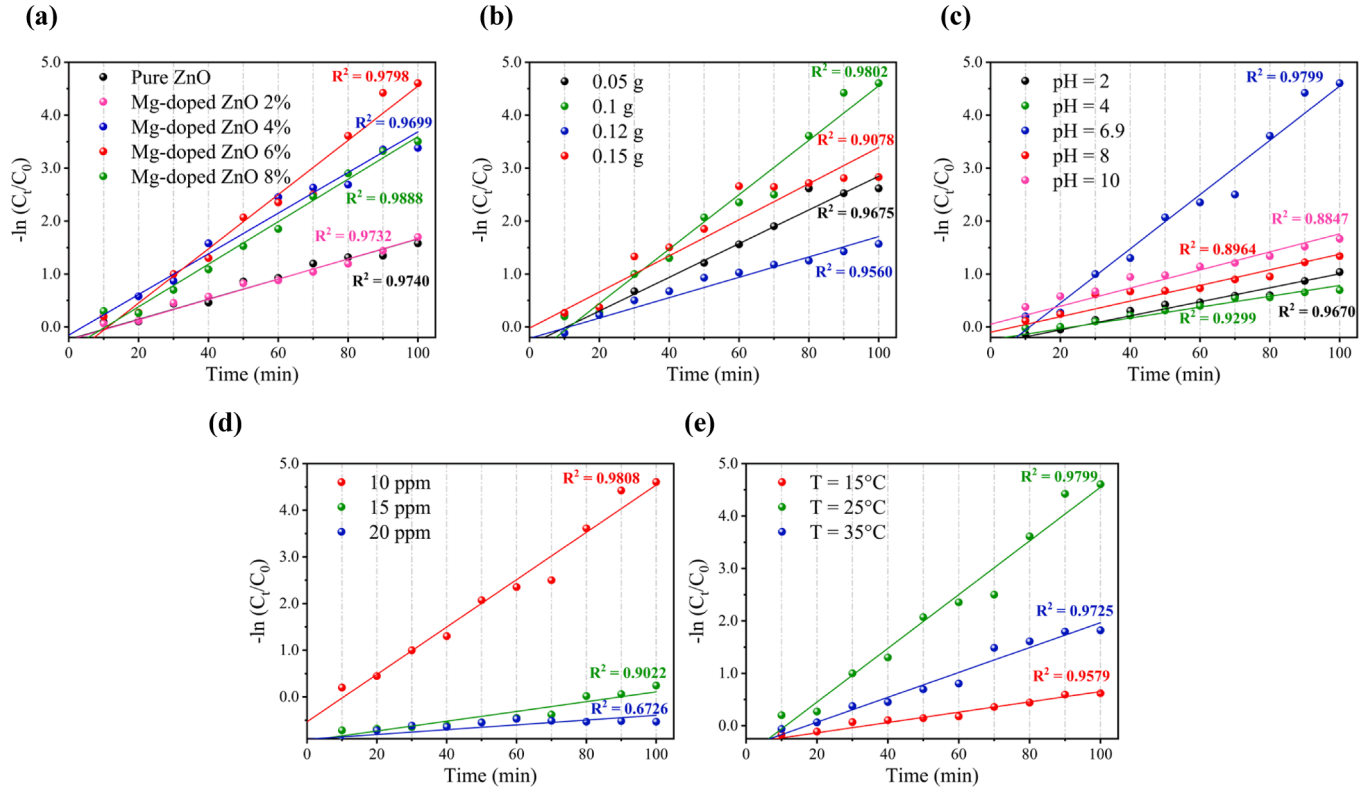


**Fig. 7.** Kinetic analysis of BF dye degradation using pure and Mg-doped ZnO nanoparticles: (a) Effect of Mg doping percentage; (b) Effect of photocatalyst mass; (c) Effect of initial solution pH; (d) Effect of initial dye concentration; and (e) Effect of reaction temperature.

to the conduction band, leaving behind holes in the valence band. These photogenerated electrons react with oxygen molecules in the solution, generating $\bullet O_2^-$, while the photogenerated holes can react with water molecules or $OH^-$ to produce •OH [106]. ROS are highly reactive and responsible for oxidizing and decomposing the dye molecules. As shown in Fig. 6 (b), increasing the Mg doping concentration from 2 % to 6 % enhances the degradation efficiency, with the 6 % Mg-doped ZnO sample achieving the highest degradation efficiency of 99.38 % within 100 min. This improvement is attributed to the increased surface area and additional active sites introduced by Mg doping, which facilitate greater adsorption of pollutant molecules and more efficient charge separation, leading to more superoxide and hydroxyl radicals [107]. However, increasing the Mg doping concentration beyond 6 %–8 % results in a slight reduction in efficiency. This decline is likely due to particle agglomeration and the formation of recombination centers, which reduce the availability of free electrons and holes necessary for effective photocatalysis, thus lowering the production of ROS like $\bullet O_2^-$ or •OH [105,108].

Additionally, the linear plots of $\ln(C_0/C)$ versus time, as shown in Fig. 7 (a), demonstrate that the degradation process follows pseudo-first-order kinetics, with high $R^2$ values confirming the model's applicability across all doping levels. The reaction rate constants, presented in Table 2, further support this observation. The Mg-doped ZnO 6 % sample exhibits the highest reaction rate constant ($k = 0.0512\ min^{-1}$), highlighting its superior photocatalytic activity. In contrast, the rate constant for the Mg-doped ZnO 8 % sample is slightly lower, reflecting the decreased efficiency due to agglomeration and charge recombination at higher doping levels, which diminishes the generation of ROS includes $\bullet O_2^-$ or •OH radicals [103,106,107].

Thus, moderate Mg doping (6 %) significantly enhances the photocatalytic degradation of BF dye by optimizing surface area and charge carrier dynamics. However, higher doping concentrations (>6%) can impede performance due to the formation of recombination centers. The kinetic data confirm that the photocatalytic degradation follows pseudo-first-order kinetics for all doping levels, with the Mg-doped ZnO 6 % sample demonstrating the highest reaction rate and overall degradation efficiency.

### 3.5.2. Effect of Mg-doped ZnO photocatalyst mass

The influence of photocatalyst mass on the degradation efficiency of BF dye using Mg-doped ZnO NPs was investigated by varying the catalyst mass from 0.05 to 0.15 g. Fig. 6 (c) illustrates the relationship between photocatalyst mass and degradation efficiency over time, while Fig. 7 (b) provides the corresponding kinetic analysis based on the pseudo-first-order model.

As depicted in Fig. 6 (c), increasing the mass of Mg-doped ZnO from 0.05 to 0.15 g led to a marked improvement in photocatalytic performance. The sample with 0.10 g of Mg-doped ZnO achieved almost complete degradation efficiencies of 94.95 %, 98 %, and 99.38 % observed for 0.05, 0.12, and 0.15 g after 100 min irradiation. This enhancement in degradation efficiency with increasing photocatalyst mass can be attributed to the larger number of active surface sites available for the photocatalytic reactions, which facilitates the generation of •OH and $\bullet O_2^-$ radicals, key intermediates in the oxidation of organic pollutants such as BF dye [105]. However, while increasing the photocatalyst mass initially enhances degradation efficiency, the results in Fig. 6 (c) suggest that after a certain mass threshold (0.12 g), the rate of improvement diminishes. This may be due to light scattering and reduced photon penetration within the reaction medium at higher catalyst concentrations, leading to less effective utilization of active sites' available light and saturation [109]. Thus, while higher catalyst masses provide more active sites, the excessive use of photocatalysts can limit the reaction efficiency due to mass agglomeration and light attenuation effects.

The pseudo-first-order kinetics of BF dye degradation were also evaluated, and the linear plots of $\ln(C_0/C)$ versus time for different Mg-doped ZnO masses are shown in Fig. 7 (b). The kinetic analysis demonstrates that the degradation process follows pseudo-first-order kinetics, with rate constants kk increasing as the photocatalyst mass increases. The rate constants for 0.05, 0.10, 0.12, and 0.15 g Mg-doped ZnO masses are 0.0192, 0.0514, 0.0341, and 0.0348 $min^{-1}$, respectively, as presented in Table 2. The highest rate constant ($k = 0.0514\ min^{-1}$) is observed for the 0.10 g sample, indicating optimal catalyst loading for efficient photocatalytic degradation. As the mass increases to 0.15 g, the rate constant slightly decreases, consistent with the observed saturation effect, where further increases in photocatalyst mass do not

**Table 2**
Summary of photocatalytic degradation efficiency, $R^2$, and reaction rate constants for BF dye degradation using pure and Mg-doped ZnO NPs.

| Parameter | Condition | Degradation (%) | $R^2$ | Rate constant $k$ ($min^{-1}$) | Uncertainty (±) |
|---|---|---|---|---|---|
| Mg doping concentration | Pure ZnO | 87.28 | 0.9641 | 0.0190 | 0.00122 |
| | Mg-doped ZnO 2 % | 88.70 | 0.9733 | 0.0191 | 0.00106 |
| | Mg-doped ZnO 4 % | 97.90 | 0.9699 | 0.0384 | 0.00225 |
| | Mg-doped ZnO 6 % | 99.38 | 0.9799 | 0.0512 | 0.00245 |
| | Mg-doped ZnO 8 % | 98.15 | 0.9888 | 0.0402 | 0.00143 |
| Photocatalyst mass (g) | 0.05 | 95.49 | 0.9675 | 0.0318 | 0.00194 |
| | 0.1 | 99.38 | 0.9802 | 0.0514 | 0.00243 |
| | 0.12 | 87.16 | 0.9560 | 0.0192 | 0.00137 |
| | 0.15 | 96.36 | 0.9078 | 0.0341 | 0.00362 |
| Solution pH | pH 2 | 78.15 | 0.9670 | 0.0133 | 0.00082 |
| | pH 4 | 69.26 | 0.9299 | 0.0103 | 0.00094 |
| | pH 6.9 (Neutral) | 99.38 | 0.9799 | 0.0512 | 0.00245 |
| | pH 8 | 83.83 | 0.8964 | 0.0147 | 0.00167 |
| | pH 10 | 88.33 | 0.8847 | 0.0171 | 0.00206 |
| Initial dye concentration (ppm) | 10 ppm | 99.38 | 0.9808 | 0.0507 | 0.00237 |
| | 15 ppm | 67.78 | 0.9022 | 0.0105 | 0.00115 |
| | 20 ppm | 47.53 | 0.6726 | 0.0052 | 0.00120 |
| Reaction temperature (°C) | 15 °C | 66.79 | 0.9579 | 0.0098 | 0.00069 |
| | 25 °C | 99.38 | 0.9799 | 0.0512 | 0.00245 |
| | 35 °C | 90.00 | 0.9725 | 0.0237 | 0.00133 |

proportionally enhance degradation efficiency due to the aforementioned light attenuation and particle agglomeration [37,109].

Consequently, the results suggest that the optimal Mg-doped ZnO photocatalyst mass for the degradation of BF dye under UV irradiation is 0.10 g, providing the highest degradation efficiency and reaction rate constant. While increasing the catalyst mass improves the degradation rate by providing more active sites, excessive amounts of photocatalyst can result in diminishing returns due to light scattering and mass agglomeration. The pseudo-first-order kinetic model effectively describes the degradation process, with a strong correlation between photocatalyst mass and reaction rate.

### 3.5.3. Effect of initial solution pH

The influence of initial solution pH on the photocatalytic degradation of BF dye was examined over a pH range of 2 to 10, with a dye concentration of 3 ppm. The results, presented in Fig. 6 (d), demonstrate that the pH of the solution significantly affects the degradation efficiency. pH is a critical factor influencing the photocatalyst's surface charge and the dye molecules' ionization state, affecting the overall adsorption and photocatalysis processes [1]. As shown in Fig. 6 (d), the degradation efficiency increases with rising pH, reaching a maximum of 99.38 % at neutral pH (6.9). The degradation efficiency is considerably lower in acidic conditions (pH 2) (78.15 %). This reduced performance at low pH levels can be attributed to the protonation of the Mg-doped ZnO surface, which creates a positively charged surface that repels the cationic BF dye molecules, thereby limiting their adsorption onto the photocatalyst [110–112].

Additionally, the competition between protons ($H^+$) and dye molecules for the available adsorption sites further reduces the photocatalytic efficiency under highly acidic conditions [113,114]. At basic pH values (pH 8 and 10), the degradation efficiency decreases again, with the lowest value (88.33 %) observed at pH 10. The reduction in degradation at higher pH can be explained by the formation of excess $OH^-$ in the solution. These hydroxide ions act as scavengers of the photo-generated holes, preventing the formation of •OH and $\bullet O_2^-$ radicals, essential for the oxidative breakdown of organic pollutants. Furthermore, the basic environment may alter the dye structure, reducing interaction with the photocatalyst surface [112,115].

The kinetic analysis of BF dye degradation at different pH levels was performed using the pseudo-first-order kinetic model. The linear plots of $\ln(C_0/C)$ versus time, shown in Fig. 7 (c), confirm that the degradation process follows pseudo-first-order kinetics across all tested pH conditions. The highest reaction rate constant, $k = 0.0512\ \text{min}^{-1}$, was observed at pH 6.9, consistent with the optimal degradation efficiency observed at this pH. The $R^2$ values for the kinetic plots, as presented in Table 2, further validate the kinetic model, with $R^2 = 0.9799$ at pH 6.9. At higher pH values, the reaction rate constant decreases, with $k = 0.0147\ \text{min}^{-1}$ at pH 8 and $k = 0.0171\ \text{min}^{-1}$ at pH 10. This decline in rate constant at basic pH levels confirms the detrimental effect of hydroxide ions on the photocatalytic process by hindering the formation of reactive radicals and altering the dye structure [111,116].

Accordingly, the results demonstrate that pH plays a crucial role in determining the photocatalytic degradation efficiency of BF dye. The optimal pH for degradation is neutral (pH 6.9), where the surface charge of the photocatalyst is balanced, allowing maximum interaction between the cationic BF dye and the negatively charged surface sites. At both highly acidic and highly basic conditions, the degradation efficiency decreases due to charge repulsion and hydroxide ion interference, respectively. The kinetic analysis further supports these findings, with the highest reaction rate constant observed at neutral pH, confirming that solution pH is a critical parameter for optimizing photocatalytic processes.

### 3.5.4. Effect of initial dye concentration

The effect of initial dye concentration on the photocatalytic degradation of BF dye was investigated at three different concentrations: 10, 15, and 20 ppm. The results, presented in Fig. 6 (e), reveal a strong dependence of the degradation efficiency on the initial dye concentration. As the initial concentration of BF dye increases, a notable decrease in degradation efficiency is observed. The highest degradation efficiency (~100 %) is achieved with a 10-ppm dye concentration, while lower efficiencies of 67.78 % and 47.53 % are recorded for 15 and 20 ppm concentrations, respectively, after 100 min of UV irradiation. The interaction between dye molecules drives the photocatalytic degradation process and •OH radicals, which are generated on the surface of the photocatalyst upon UV light exposure. At lower dye concentrations (10 ppm), the availability of hydroxyl radicals is sufficient to ensure efficient interaction with the dye molecules, resulting in complete degradation. However, at higher dye concentrations (15 and 20 ppm), the increased number of dye molecules competes for the limited number of active sites on the catalyst surface. This reduces the formation of •OH and $\bullet O_2^-$ radicals as the catalyst surface becomes saturated with dye molecules, thereby inhibiting the degradation process. The excess dye also absorbs more UV light, reducing the effective light reaching the catalyst surface and further hindering the generation of reactive species [117].

The pseudo-first-order kinetic model was applied to describe the degradation process at different initial dye concentrations, as shown in Fig. 7 (d). The linearity of the plots for each concentration confirms that the degradation follows pseudo-first-order kinetics, with higher dye concentrations exhibiting slower reaction rates. The reaction rate constants for 10, 15, and 20 ppm are 0.0507, 0.0105, and 0.0052 $\text{min}^{-1}$, respectively, as presented in Table 2. The highest rate constant is observed for the 10-ppm concentration, corresponding to the fastest degradation process. The rate constants decrease significantly as the initial dye concentration increases, with the 20-ppm solution exhibiting the lowest rate constant. This reduction in reaction rate is due to the limited availability of hydroxyl radicals and active sites on the catalyst surface, which are essential for the photocatalytic process [116,118]. Furthermore, the $R^2$ values for the kinetic plots demonstrate a strong correlation between the pseudo-first-order model and the experimental data, particularly for the 10-ppm concentration ($R^2 = 0.9808$).

Hence, the results highlight that lower initial dye concentrations result in more efficient photocatalytic degradation, with the optimal concentration for BF dye removal being 10 ppm. At higher concentrations (15 and 20 ppm), the degradation efficiency decreases due to the saturation of active sites on the photocatalyst surface and reduced availability of hydroxyl radicals. The kinetic analysis confirms that the degradation follows pseudo-first-order kinetics, with the reaction rate decreasing as the initial dye concentration increases. These findings underscore the importance of optimizing dye concentration in photocatalytic processes to maximize degradation efficiency and reaction rates.

### 3.5.5. Effect of reaction temperature

The influence of reaction temperature on the photocatalytic degradation of BF dye was assessed by performing experiments at 15, 25, and 35 °C. Fig. 6 (f) shows that increasing the reaction temperature generally enhances the degradation efficiency. The highest degradation efficiency was observed at 25 °C, where 99.38 % of the dye was degraded after 100 min of UV irradiation. In comparison, 90 % and 66.79 % degradation efficiencies were recorded at 35 and 15 °C, respectively. The enhanced degradation efficiency at 25 °C can be attributed to the optimal balance between the kinetic energy of the BF dye molecules and the mobility of photo-generated charge carriers (electrons and holes) at this moderate temperature. At higher temperatures (e.g., 35 °C), while charge carrier mobility improves, factors such as potential thermal deactivation of the photocatalyst and particle agglomeration may begin to counteract these benefits, slightly reducing the overall degradation efficiency [118–120]. Conversely, at 15 °C, the lower kinetic energy of the dye molecules and reduced charge carrier mobility hinder the photocatalytic process, leading to the lowest degradation efficiency.

The kinetic analysis in Fig. 7 (e) further supports the observed

temperature effects on photocatalytic activity. The linear plots of $\ln(C_0/C)$ versus time for different temperatures confirm that the degradation follows pseudo-first-order kinetics across all conditions. The reaction rate constants derived from the slopes of these plots reveal a temperature-dependent increase in reaction rate, with the highest rate constant observed at 25 °C ($k = 0.0512\ \text{min}^{-1}$). In contrast, lower rate constants were recorded at 35 °C ($k = 0.0237\ \text{min}^{-1}$) and 15 °C ($k = 0.0098\ \text{min}^{-1}$), as summarized in Table 2. Although the reaction rate at 35 °C is higher than at 15 °C, the slight reduction in degradation efficiency compared to 25 °C can be explained by potential drawbacks at elevated temperatures, such as thermal deactivation or agglomeration of catalyst particles. These effects reduce the available surface area for photocatalytic reactions, thus explaining why 25 °C provides the most favorable conditions for photocatalytic degradation in this study.

Therefore, this study demonstrates the significant impact of reaction temperature on the photocatalytic degradation of BF dye. While higher temperatures generally improve photocatalytic activity by enhancing charge carrier mobility and dye diffusion, 25 °C was the optimal temperature, yielding the highest degradation efficiency (~100 %) after 100 min. A slight reduction in efficiency at 35 °C highlights the importance of balancing thermal effects to avoid potential deactivation or agglomeration. Thus, controlling reaction temperature is essential for optimizing photocatalytic systems for effective pollutant degradation.

As a result, the photocatalytic degradation of BF dye using Mg-doped ZnO NPs was systematically studied under various experimental conditions, including Mg doping percentage, photocatalyst mass, initial solution pH, dye concentration, and reaction temperature. The findings demonstrated that each parameter significantly influences degradation efficiency and reaction kinetics. Optimal photocatalytic performance was achieved at a Mg doping concentration of 6 %, a photocatalyst mass of 0.10 g, a neutral pH of 6.9, a dye concentration of 10 ppm, and a reaction temperature of 25 °C. Under these conditions, the highest degradation efficiency and the fastest reaction rates were observed, with degradation following pseudo-first-order kinetics across all tested scenarios. These results emphasize the critical role of optimizing experimental parameters to enhance photocatalytic activity, particularly for environmental applications that effectively remove organic pollutants.

### 3.6. Comparative study

A comparative analysis was conducted with other metal-doped ZnO systems reported in the literature to evaluate the photocatalytic performance of Mg-doped ZnO NPs synthesized via co-precipitation. The focus was on studies where co-precipitation methods were used, as this technique is widely recognized for its simplicity and ability to produce uniformly doped ZnO nanoparticles. Co-precipitation allows for a homogeneous distribution of dopants within the ZnO lattice, enhancing photocatalytic properties [121,122].

Table 3 presents a comparative summary of photocatalytic degradation efficiencies for various metal-doped ZnO NPs. The current study achieved a ~100 % degradation efficiency for BF under UV light irradiation with a catalyst dose of 0.1 g and a reaction time of 100 min. Undoped ZnO under the same conditions exhibited a degradation efficiency of 87.28 %. These results are consistent with those of Moulahi [123], where Mg-doped ZnO showed a 98 % efficiency for Rhodamine B (RhB) degradation, compared to 13 % for pure ZnO. The improved performance of Mg-doped ZnO is attributed to reduced electron-hole recombination rates and increased surface area, providing more active sites for photocatalytic reactions. This highlights the effectiveness of Mg as a dopant in enhancing ZnO's photocatalytic performance across various dye pollutants.

Noble metal doping enhances the photocatalytic efficiency of semiconductors like ZnO, primarily due to the surface plasmon resonance (SPR) effect, which increases visible light absorption. For instance, Ahmad et al. [124] reported that Au-doped ZnO achieved a 95 % degradation of RhB in 180 min using 0.03 g of catalyst, compared to 74 % for pure ZnO. Similarly, Pathak et al. [125] reported that Ag-doped ZnO showed a 45 % degradation efficiency for Methylene Blue (MB), compared to 8 % for pure ZnO under UV light. These improvements are attributed to enhanced charge separation and prolonged electron-hole lifetimes, which boost the generation of ROS. Although the mechanisms differ, with Mg doping modifying the band gap and noble metals enhancing photocatalysis via SPR, both approaches yield high degradation efficiencies, comparable to the current study's findings with Mg-doped ZnO.

**Table 3**
Comparative summary of photocatalytic efficiency of metal-doped ZnO NPs synthesized via co-precipitation.

| Dopant element | Target Pollutant | Time (min) | Catalyst dose (g) | Degradation efficiency (%) | | Reference |
|---|---|---|---|---|---|---|
| | | | | Pure ZnO | Doped ZnO | |
| Mg | Methylene Blue (MB) | 100 | 0.06 | | 55 | [83] |
| Cu | Crystal Violet (CV) | 210 | 0.25 | 48.19 | 78.7 | [126] |
| IZ | Rhodamine B (RhB) | 120 | 0.05 | 8 | 76 | [128] |
| Cu | Methyl Orange (MO) | 120 | 0.3 | | 99 | [129] |
| Sb | MB | 120 | 0.03 | | 84 | [130] |
| Au | MB | 160 | 0.02 | 8 | 25 | [125] |
| Ag | MB | 160 | 0.02 | 8 | 45 | [125] |
| Sm | MB | 90 | 0.025 | 57 | 96 | [130] |
| Mn | MB | 120 | 0.02 | 19 | 81 | [127] |
| Co | MB | 120 | 0.02 | 19 | 48 | [127] |
| Zr | MB | 30 | 0.07 | 90 | 97 | [131] |
| Mg | RhB | 120 | 1 | 13 | 98 | [123] |
| Au | RhB | 180 | 0.3 | 74 | 95 | [124] |
| **Mg** | **BF** | **100** | **0.1** | **87.28** | **99.38** | **This study** |

Transition metals, including Cu, Mn, and Co, have also been extensively studied for their photocatalytic properties when used to dope ZnO. Mittal et al. [126] reported that Cu-doped ZnO achieved a 78.7 % degradation efficiency for Crystal Violet (CV) and 99 % for Methyl Orange (MO) with 0.25 g and 0.3 g catalyst doses, respectively. In contrast, pure ZnO exhibited much lower degradation efficiencies of 48.19 % for CV and 30 % for MO. Qi et al. [127] found that Mn-doped ZnO displayed an 81 % efficiency for MB degradation compared to 19 % for pure ZnO. While Co-doped ZnO showed a relatively lower efficiency (48 %), it still significantly outperformed pure ZnO (19 %). The increased efficiencies of Cu, Mn, and Co-doped systems are mainly due to enhanced charge carrier mobility and reduced electron-hole recombination. In comparison, Mg-doped ZnO in this study demonstrates even higher degradation efficiency for BF, indicating that Mg is a more versatile dopant for a broader range of photocatalytic applications.

Besides, doping with rare earth metals such as Zr and Sb has notably improved ZnO's photocatalytic performance [132]. Długosz et al. [131] reported that Zr-doped ZnO achieved 97 % degradation of MB in just 30 min with a catalyst dose of 0.07 g, compared to 90 % for pure ZnO. Similarly, Jagadhesan et al. [130] found that Sb-doped ZnO reached an efficiency of 84 % for MB in 120 min with 0.03 g of catalyst, a significant increase from 19 % for pure ZnO. The improvement in photocatalytic activity with Zr and Sb is attributed to the formation of oxygen vacancies and enhanced light absorption due to the increased surface area. These results are consistent with the findings in this study, where Mg-doped ZnO showed remarkable photocatalytic activity for BF degradation, with an efficiency of 99.38 %. This suggests that Mg doping is as effective as, or even superior to, rare earth metal doping in some cases, especially for the degradation of cationic dyes like BF. Subsequently, this comparative analysis underscores the significant impact of doping ZnO with various metals on its photocatalytic efficiency. Mg-doped ZnO

stands out as one of the most efficient photocatalysts for the degradation of organic dyes, achieving 99.38 % degradation of BF in this study and showing consistently high performance across different dyes in the literature. Noble metals such as Au and Ag provide significant enhancements through the SPR effect, while transition metals like Cu and Mn improve charge separation and recombination rates. Rare earth metals like Zr and Sb further boost photocatalytic activity by creating oxygen vacancies and increasing surface area. The results from this study suggest that Mg-doped ZnO is highly competitive and, in some cases, superior to other metal-doped ZnO systems, making it an ideal candidate for environmental applications, particularly in the degradation of toxic organic pollutants.

### 3.7. DFT analysis and computational insights

DFT calculations were employed to elucidate further the mechanisms responsible for the enhanced photocatalytic activity observed in the experimental results of Mg-doped ZnO. The optimized structure of the Mg-doped ZnO cluster, designed to model the optimal Mg doping concentration of 6 %, was utilized to simulate the interaction with BF dye. This computational model provides detailed insights into the electronic properties, charge distribution, and non-covalent interactions between the Mg-doped ZnO cluster and the dye molecule.

#### 3.7.1. Structural insights

Fig. 8 (a) presents the optimized structure of the Mg-doped ZnO cluster, demonstrating its interaction with the BF dye molecule. This cluster, designed to simulate the experimentally observed 6 % Mg-doped ZnO sample, includes a lattice framework consisting of hexagonal (six-membered rings) and tetragonal (four-membered rings). These structural motifs are essential for maintaining the stability and reactivity of the ZnO surface during photocatalytic reactions. The Mg atoms, represented in green, substitute Zn atoms within the lattice, particularly around the tetragonal rings. This substitution causes local geometric distortions, modifying the electronic density in the surrounding regions and introducing new active sites for the interaction with organic pollutants like BF dye. The Mg doping enhances the surface reactivity of ZnO by modifying the electron distribution within the hexagonal and tetragonal rings, creating electron-rich regions that act as enhanced adsorption sites for dye molecules [91,102]. These modifications

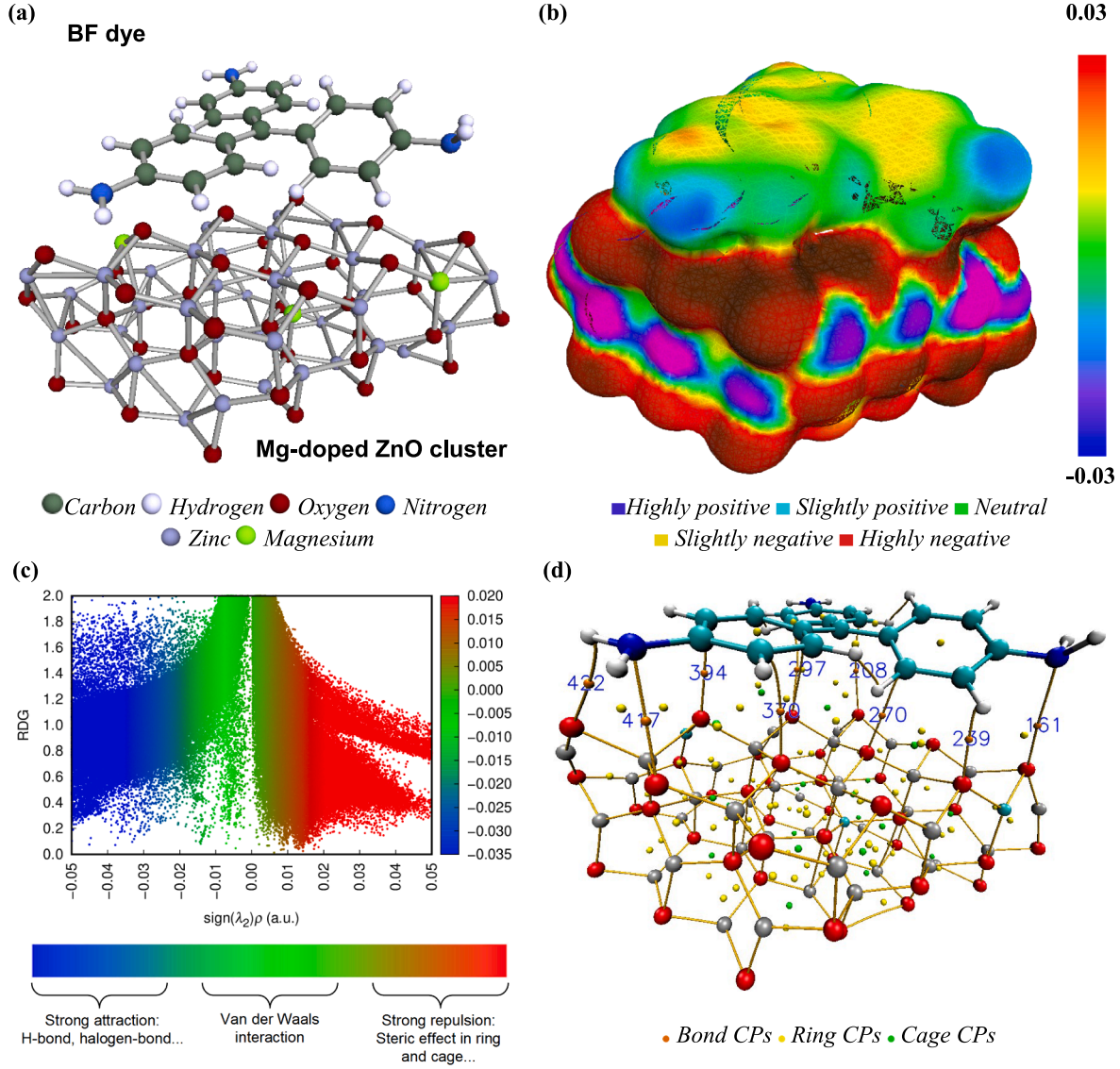


**Fig. 8.** (a) Optimized structure of Mg-doped ZnO cluster interacting with BF dye molecule, (b) COSMO-RS charge distribution visualizing surface reactivity, (c) RDG scatter plot highlighting non-covalent interactions within the Mg-doped ZnO@BF complex, and (d) QTAIM molecular graph illustrating bond, ring, and cage critical points (CPs) in the interaction network between Mg-doped ZnO and BF dye.

promote efficient charge transfer and adsorption, facilitating stronger interactions between the catalyst and the dye molecules. The substitution of Zn by Mg creates localized electronic states that enhance charge separation, thereby reducing the recombination of electron-hole pairs, a critical factor in promoting the generation of ROS such as •OH, which drives the oxidative degradation of BF dye.

### 3.7.2. COSMO-RS charge distribution

The COSMO-RS charge distribution analysis offers critical insights into the Mg-doped ZnO cluster's reactivity and surface interaction potential, particularly in its interaction with BF dye during photocatalytic degradation. As illustrated in Fig. 8 (b), the surface charge distribution varies from highly positive (blue) to highly negative (red) regions, providing valuable predictions about where key degradation reactions are likely to occur. The highly positive regions (blue/purple) represent electron-deficient zones, crucial for attracting negatively charged species, such as ROS generated during photocatalysis. These regions are significantly influenced by Mg doping, which alters the electronic environment within the ZnO lattice by replacing Zn atoms, thereby creating new active sites that enhance the material's adsorption capacity for pollutants [62,133–135]. Neutral to slightly positive regions (green) facilitate intermediate charge transfer processes, stabilizing the adsorption of dye molecules and preventing rapid recombination of electron-hole pairs. These regions are critical in maintaining the catalyst's reactivity during continuous photocatalysis [133].

On the other hand, highly negative regions (red/orange) correspond to electron-rich zones, ideal for nucleophilic reactions, particularly involving ROS like •OH, which are instrumental in breaking down the dye molecules. These findings align with experimental observations, where Mg-doped ZnO demonstrated superior photocatalytic activity compared to undoped ZnO. The COSMO-RS analysis, thus, underscores the significant role of charge redistribution induced by Mg doping, which optimizes electron transfer and enhances pollutant-catalyst interactions. COSMO-RS complements experimental data by visually representing the most reactive sites, offering a deeper understanding of how Mg-doped ZnO achieves high photocatalytic efficiency through improved charge separation and surface reactivity [136,137]. These computational insights, supported by published works, demonstrate the substantial improvement in degradation performance attributed to Mg doping [123,124].

### 3.7.3. NCI-RDG analysis

NCI, such as Van der Waals forces and hydrogen bonding, are fundamental to understanding the molecular interactions that drive photocatalytic systems [133]. The RDG analysis, paired with color-coded scatter plots, provides an advanced visualization of regions dominated by these weak interactions [63,138–142]. Fig. 8 (c) presents the RDG scatter plot for the Mg-doped ZnO cluster in interaction with BF dye, showcasing the varying strengths of these interactions. The blue regions in the plot indicate strong, attractive forces, particularly hydrogen bonds, which play a critical role in anchoring dye molecules to the catalyst surface and ensuring efficient adsorption. Halogen bonds, if present, also contribute to these strong interactions. Green regions represent moderate Van der Waals forces, essential for maintaining the proximity of dye molecules to the catalyst's active sites without strong covalent bonding. While weaker than hydrogen bonds, these interactions facilitate continuous contact between the dye and the photocatalyst, promoting effective electron transfer. Finally, the red regions signify areas of strong steric repulsion, which prevent molecular crowding and ensure that active sites on the catalyst surface remain accessible. This balance between attractive and repulsive forces is critical for the system's overall photocatalytic efficiency. The RDG analysis confirms the presence of these essential non-covalent interactions in the Mg-doped ZnO system, which significantly contribute to the high photocatalytic performance observed experimentally. These interactions, particularly the hydrogen bonding and Van der Waals forces, stabilize the dye molecules on the catalyst surface, facilitating charge transfer and enhancing degradation efficiency. The NCI-RDG analysis is, therefore, instrumental in providing a comprehensive understanding of how these weak forces influence the photocatalytic degradation of organic pollutants, corroborating results found in similar studies [83].

### 3.7.4. QTAIM analysis and bond critical points (BCPs)

QTAIM analysis provides a deeper understanding of the bonding interactions within the Mg-doped ZnO and BF dye complex. This analysis focuses on key features at BCPs, which serve as indicators of significant bonding interactions. Table 4 summarizes the topological characteristics of selected BCPs within the Mg-doped ZnO@BF complex. Parameters such as electron density ($\rho(r)$), Laplacian of electron density ($\nabla^2\rho(r)$), potential energy density ($V(r)$), kinetic energy density ($G(r)$), and the ratio of potential to kinetic energy density ($|V(r)|/G(r)$) are analyzed to quantify the strength and nature of the bonding interactions [134,143–145]. Notably, higher $\rho(r)$ values and negative $V(r)$ values at BCPs indicate strong hydrogen bonding interactions, critical in facilitating BF dye adsorption and degradation. For example, BCPs such as 161 and 239 exhibit significant electron density, indicating robust hydrogen bonding between BF dye and the Mg-doped ZnO surface. These strong interactions contribute to the enhanced photocatalytic efficiency observed experimentally. The potential energy density values at these BCPs further highlight the strength of these attractive interactions, correlating with the high degradation efficiency reported in experimental studies. The molecular graph in Fig. 8 (d) visualizes the distribution of bond critical points, ring critical points, and cage critical points, reinforcing the presence of strong interactions that facilitate the catalytic degradation pathway of BF dye. This QTAIM analysis, in conjunction with the experimental results, validates the critical role of these bonding interactions in the high photocatalytic performance of Mg-doped ZnO.

Consequently, the DFT analysis, combined with COSMO-RS, RDG, and QTAIM insights, provides a comprehensive understanding of the molecular interactions driving the high photocatalytic activity of Mg-doped ZnO. These computational results align with the experimental findings, highlighting the crucial role of Mg doping in enhancing electron transfer, charge separation, and reactive oxygen species generation. By optimizing the interactions between the catalyst surface and BF dye molecules, Mg-doped ZnO demonstrates exceptional potential for environmental remediation applications, particularly in the degradation of organic pollutants.

### 3.7.5. Photodegradation mechanism

The photocatalytic degradation mechanism of BF dye using Mg-doped ZnO NPs is illustrated in Fig. 9. This mechanism is developed based on a combination of experimental findings and DFT insights, elucidating the critical role of Mg doping in enhancing ZnO's photocatalytic efficiency. Upon UV light irradiation, electrons in the ZnO are excited from the valence band (VB) to the conduction band (CB), generating electron-hole pairs ($e^-$/ $h^+$) that drive the photocatalytic process. In Mg-doped ZnO, the doped Mg atoms act as efficient electron traps by substituting Zn atoms within the lattice, significantly reducing the recombination rate of photo-generated electron-hole pairs, a common issue in pure ZnO systems [146]. The trapped electrons are then transferred from the CB to surface-adsorbed oxygen molecules, reducing them to $\bullet O_2^-$, which are highly ROS responsible for initiating the oxidative degradation of organic pollutants like BF dye [105,108]. Simultaneously, the photo-generated holes ($h^+$) migrate to the ZnO surface, where they react with water molecules or $OH^-$ ions in the solution, generating •OH. These •OH radicals are powerful oxidizing agents that attack the dye molecules, breaking down their complex structure into smaller degradation products. The involvement of both $\bullet O_2^-$ and •OH as active ROS highlights the synergistic role of Mg doping in enhancing ROS generation.

The valence band (VB) and conduction band (CB) edge potentials of

**Table 4**
Topological parameters of the interaction sites (in a.u.) at selected BCPs in Mg-doped ZnO@BF complex.

| BCP | X–Y | ρ(r) | $\nabla^2\rho(r)$ | V(r) | G(r) | \|V(r)\|/G(r) | H(r) |
|---|---|---|---|---|---|---|---|
| **161** | 9(O)–88(N) | 0.000464 | 0.002796 | −0.000187 | 0.000443 | −0.422570 | 0.000256 |
| **208** | 3(O)–99(C) | 0.002259 | 0.007742 | −0.001001 | 0.001468 | −0.681853 | 0.000467 |
| **239** | 20(O)–114(H) | 0.007089 | 0.027447 | −0.004318 | 0.005590 | −0.772462 | 0.001272 |
| **270** | 17(O)–95(C) | 0.006888 | 0.024906 | −0.003672 | 0.004949 | −0.741861 | 0.001278 |
| **297** | 14(O)–97(C) | 0.003388 | 0.011872 | −0.001662 | 0.002315 | −0.717962 | 0.000653 |
| **370** | 28(O)–102(C) | 0.006642 | 0.019462 | −0.003312 | 0.004089 | −0.809990 | 0.000777 |
| **394** | 25(O)–104(C) | 0.012102 | 0.038020 | −0.007531 | 0.008518 | −0.884097 | 0.000987 |
| **417** | 39(O)–86(N) | 0.008341 | 0.026081 | −0.005667 | 0.006093 | −0.929954 | 0.000427 |
| **422** | 36(O)–119(H) | 0.005000 | 0.021178 | −0.003384 | 0.004339 | −0.779813 | 0.000955 |

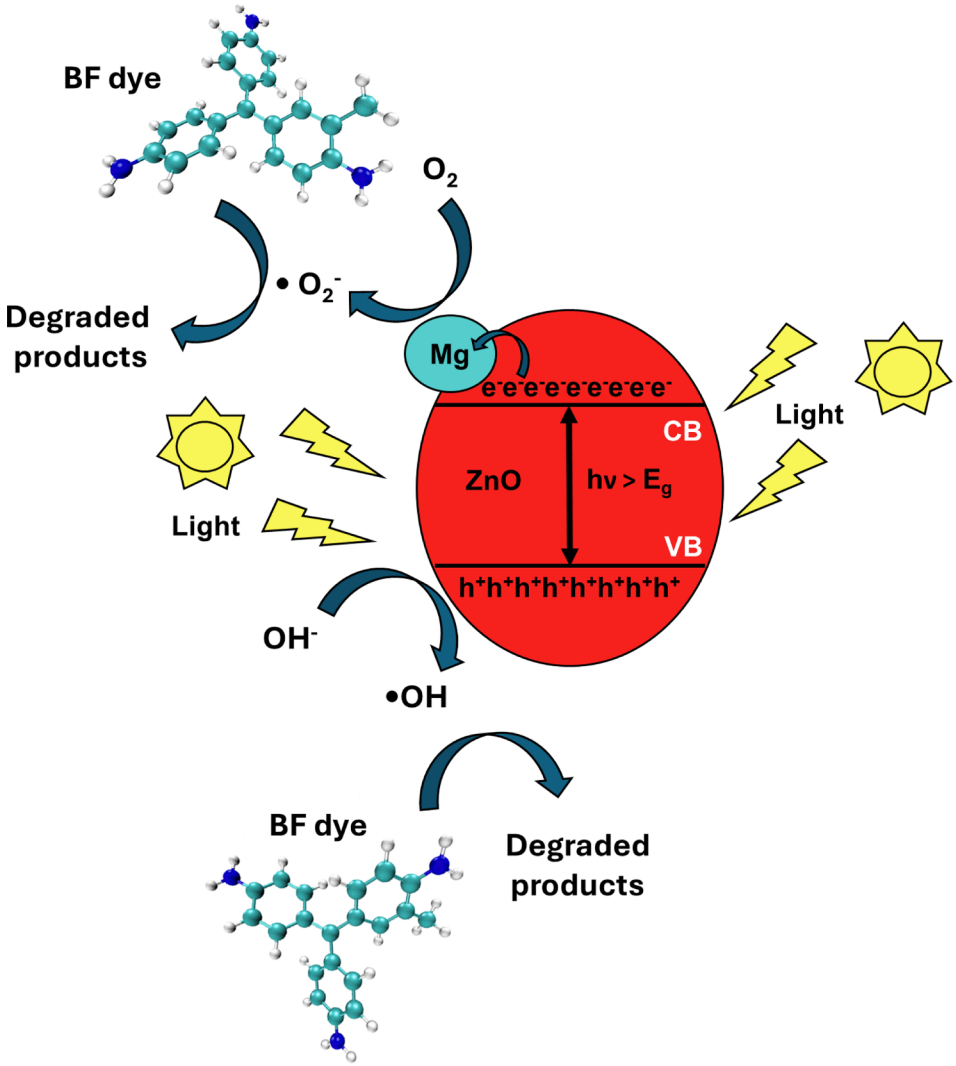


**Fig. 9.** Proposed photocatalytic degradation mechanism of BF dye by Mg-doped ZnO NPs under UV light irradiation.

pure and Mg-doped ZnO nanoparticles were calculated using the Mulliken electronegativity approach to elucidate the charge transfer dynamics and the enhanced photocatalytic activity. The band edge potentials were calculated using the following equations [147,148]:

$$E_{CB} = X - E_e - \frac{E_g}{2} \quad (5)$$

$$E_{VB} = E_{CB} - E_g \quad (6)$$

X is the absolute electronegativity of ZnO (5.79 eV), $E_e$ is the energy of free electrons on the hydrogen scale (4.5 eV), and $E_g$ is the band gap energy obtained from the Tauc plots shown in Fig. 5. The calculated band gap values are 3.68 eV for pure ZnO, 3.16 eV for 2 % Mg-doped ZnO, 3.26 eV for 4 % Mg-doped ZnO, 3.41 eV for 6 % Mg-doped ZnO, and 3.52 eV for 8 % Mg-doped ZnO. The calculated CB and VB edge potentials are summarized in Table 5 using these values

These calculated band edge positions indicate that the CB potentials for all Mg-doped ZnO samples are more negative than the reduction potential of $O_2/\bullet O_2^-$ (−0.33 V vs. NHE), confirming the capability of photogenerated electrons to reduce oxygen molecules into highly reactive $\bullet O_2^-$ radicals. Concurrently, the VB potentials are more favorable than the oxidation potential of $H_2O/\bullet OH$ (+2.38 V vs. NHE), indicating

**Table 5**
Calculated Conduction Band and Valence Band edge potentials for pure and Mg-doped ZnO NPs.

| Sample | $E_{CB}$ (eV) | $E_{VB}$ (eV) |
|---|---|---|
| Pure ZnO | −0.55 | +3.13 |
| 2 % Mg-doped ZnO | −0.74 | +2.42 |
| 4 % Mg-doped ZnO | −0.68 | +2.58 |
| 6 % Mg-doped ZnO | −0.59 | +2.82 |
| 8 % Mg-doped ZnO | −0.53 | +2.99 |

that the photo-generated holes possess sufficient oxidation power to generate •OH radicals from surface-adsorbed $OH^-$ ions. The alignment of these band edge potentials supports forming a Z-scheme heterojunction mechanism, where the photogenerated electrons in the CB of ZnO interact with holes in the VB of the Mg-doped sites. This Z-scheme charge transfer facilitates enhanced charge separation, minimizes recombination, and promotes efficient ROS generation. The band gap variation observed in the Tauc plots further supports the Z-scheme heterojunction mechanism. The redshift in the band gap at 2 % Mg doping (3.16 eV) suggests enhanced visible light absorption and increased generation of ROS, primarily due to improved charge separation and minimized recombination. However, with increasing Mg concentrations (4 %, 6 %, and 8 %), a blue shift in the band gap is observed, attributed to the Burstein-Moss effect. This shift results from band filling due to increased carrier concentration, widening the optical band gap. As illustrated in Fig. 9, the proposed mechanism involves a series of redox reactions. Under UV light irradiation, the photogenerated electrons in the CB of Mg-doped ZnO reduce oxygen molecules adsorbed on the surface to $\bullet O_2^-$ radicals, initiating the oxidative degradation of BF dye molecules. Concurrently, the photo-generated holes in the VB oxidize water molecules or surface-adsorbed $OH^-$ ions, generating •OH radicals, which further attack the dye molecules, breaking down their complex structure into more straightforward degradation products. The presence of Mg enhances this process by acting as a mediator that facilitates electron mobility and minimizes electron-hole recombination. This Z-scheme mechanism promotes efficient charge separation and enhances ROS formation, leading to the superior photocatalytic degradation performance observed experimentally.

Thus, this comprehensive mechanism, supported by experimental observations and DFT calculations, conclusively demonstrates that Mg-doped ZnO nanoparticles are highly effective in photocatalytically degrading organic pollutants like BF dye. The key to superior photocatalytic performance is the synergy between Z-scheme charge transfer, enhanced ROS generation, and optimized surface interactions. The calculated band edge potentials and proposed Z-scheme heterojunction mechanism comprehensively explain the improved photocatalytic activity, advancing the fundamental understanding of the photocatalytic mechanism. These findings underscore the potential of Mg-doped ZnO as a highly efficient photocatalyst for environmental remediation applications, particularly in the degradation of organic pollutants.

## 4. Conclusion

This study successfully demonstrated the synthesis of Mg-doped ZnO nanoparticles via a co-precipitation method, with doping concentrations ranging from 2 % to 8 %. Comprehensive characterization using XRD, SEM, FTIR, and UV–visible spectroscopy revealed significant structural, morphological, and optical modifications induced by Mg doping. XRD analysis confirmed the effective incorporation of $Mg^{2+}$ ions into the ZnO lattice, as evidenced by lattice parameter shifts and a reduction in crystallite size from 30.91 nm (pure ZnO) to 18.10 nm at 6 % Mg doping. SEM images showed uniform morphology and reduced agglomeration at optimal doping levels, while FTIR spectra identified characteristic Zn–O and Mg–O bonding vibrations, confirming structural modifications. UV–Vis spectroscopy demonstrated enhanced optical properties, with the band gap energy decreasing from 3.68 eV (pure ZnO) to 3.16 eV at 6 % Mg doping, indicating improved photocatalytic potential.

The photocatalytic degradation of Basic Fuchsin (BF) dye under UV light irradiation showed that Mg-doped ZnO nanoparticles significantly outperformed undoped ZnO. The highest degradation efficiency of 99.38 % was achieved at 6 % Mg doping within 100 min under optimal conditions: pH 6, 0.1 g catalyst mass, and an initial dye concentration of 10 ppm. These findings highlight the critical role of Mg doping in enhancing photocatalytic activity, likely due to improved electron-hole pair separation and increased generation of reactive oxygen species (ROS).

To complement the experimental results, Density Functional Theory (DFT) simulations were conducted, incorporating COSMO-RS, Reduced Density Gradient (RDG), and Quantum Theory of Atoms in Molecules (QTAIM) analyses. The DFT results revealed that Mg doping induces significant charge redistribution and enhances the interaction between the photocatalyst surface and dye molecules. Improved charge separation at Mg-doped sites and stronger dye adsorption were key factors driving the enhanced photocatalytic performance. Simulations further confirmed that Mg doping facilitates more efficient electron transfer and promotes ROS formation, aligning well with the observed experimental efficiencies.

In conclusion, this study provides a comprehensive understanding of how Mg doping enhances the photocatalytic efficiency of ZnO nanoparticles. Both experimental and theoretical analyses demonstrate that Mg-doped ZnO is an exceptionally effective photocatalyst for degrading organic pollutants such as Basic Fuchsin dye. Its enhanced photocatalytic activity, tunable optical properties, and optimized surface interactions position Mg-doped ZnO as a promising material for environmental remediation, particularly in wastewater treatment.

Building on these findings, future work will explore the scalability of these nanoparticles for industrial wastewater treatment and investigate their photocatalytic mechanisms under varying environmental conditions, including different light sources and pollutant types. Furthermore, the impact of pH at the point of zero charge ($pH_{pzc}$) on photocatalytic efficiency will be examined to understand the influence of surface charge dynamics better. Additionally, we plan to perform scavenger tests to identify the active radicals responsible for the enhanced photocatalytic activity. Specifically, quenchers such as isopropanol for hydroxyl radicals (•OH), benzoquinone for superoxide radicals ($\bullet O_2^-$), and EDTA for photogenerated holes ($h^+$) will be used to elucidate the degradation mechanism. This continued research will further advance the application potential of Mg-doped ZnO nanoparticles in environmental remediation technologies.

## CRediT authorship contribution statement

**Farida Khammar:** Writing – original draft, Visualization, Validation, Supervision, Project administration, Methodology, Investigation, Formal analysis, Conceptualization. **Said Boukerche:** Writing – original draft, Visualization, Supervision, Project administration, Methodology, Investigation, Formal analysis, Conceptualization. **Selma Djaber:** Conceptualization, Methodology, Formal analysis, Data curation, Writing – original draft, Writing – review & editing. **Abir Boublia:** Writing – review & editing, Writing – original draft, Visualization, Validation, Methodology, Investigation, Formal analysis, Conceptualization. **Abdessalam Messabhia:** Conceptualization, Methodology, Formal analysis, Data curation, Writing – original draft, Writing – review & editing. **Amel Gharbi:** Conceptualization, Methodology, Formal analysis, Data curation, Writing – original draft, Writing – review & editing. **Hana Ferkous:** Writing – review & editing, Investigation. **Cristian Vacacela Gomez:** Conceptualization, Methodology, Formal analysis, Data curation, Writing – original draft, Writing – review & editing. **Stefano Bellucci:** Conceptualization, Methodology, Formal analysis, Data curation, Writing – original draft, Writing – review & editing. **Malik Albrahim:** Formal analysis, Writing – review & editing.

**Manawwer Alam:** Conceptualization, Methodology, Formal analysis, Data curation, Writing – original draft, Writing – review & editing. **Yacine Benguerba:** Writing – review & editing, Visualization, Validation, Supervision, Software, Project administration, Investigation, Formal analysis, Conceptualization.

## Declaration of competing interest

The authors declare that they have no known competing financial interests or personal relationships that could have appeared to influence the work reported in this paper.

## Acknowledgment

Stefano Bellucci wishes to thank the Romanian Pnrr projects investment i8 Project "Composite materials for the applications in the water management field," Financing contract number: 760270/26.03.2024.

## Data availability

No data was used for the research described in the article.

## References

[1] P.O. Ukaogo, U. Ewuzie, C. V Onwuka, Environmental pollution: causes, effects, and the remedies, in: Microorg. Sustain. Environ. Heal., Elsevier, 2020: pp. 419–429.
[2] M. Erdoğan, S. Horoz, Synthesis and characterization of a triphenylamine-dibenzosuberenone-based conjugated organic material and an investigation of its photovoltaic properties, J. Chem. Res. 45 (2021) 207–212.
[3] R. Kishor, D. Purchase, L.F.R. Ferreira, S.I. Mulla, M. Bilal, R.N. Bharagava, Environmental and Health Hazards of Textile Industry Wastewater Pollutants and Its Treatment Approaches, in: Handb. Environ. Mater. Manag., 8762v, 2020: pp. 1–24. DOi: 10.1007/978-3-319-58538-3_230-1.
[4] R. Kishor, D. Purchase, G.D. Saratale, R.G. Saratale, L.F.R. Ferreira, M. Bilal, R. Chandra, R.N. Bharagava, Ecotoxicological and health concerns of persistent coloring pollutants of textile industry wastewater and treatment approaches for environmental safety, J. Environ. Chem. Eng. 9 (2021) 105012.
[5] A. Mohammadi, M. Ghaedi, M.M. Sabzehmeidani, Comparative study of malachite green adsorption onto activated carbon prepared from Ziziphus wood and ZnO nanoparticles loaded AC: artificial neural network modeling and optimization, Desalin. Water Treat. 127 (2018) 343–353.
[6] W.U. Khan, S. Ahmed, Y. Dhoble, S. Madhav, A critical review of hazardous waste generation from textile industries and associated ecological impacts, J. Indian Chem. Soc. 100 (2023) 100829.
[7] M.M. Higgins, M.T. González, J. Rojas, Enhanced X-RAYS degradation of methylene blue in the presence of gold microspheres, Radiat. Phys. Chem. 156 (2019) 73–80.
[8] P. Chowdhary, R.N. Bharagava, S. Mishra, N. Khan, Role of industries in water scarcity and its adverse effects on environment and human health, Environ. Concerns Sustain. Dev. Vol. 1 Air, Water Energy Resour. (2020) 235–256.
[9] S.-J. Young, S.-J. Chang, L. Yi-Hsing, Advanced nanomaterials for applications in photonic and sensor devices, J. Nanomater. 2022 (2022).
[10] F. Qiao, K. Sun, H. Chu, J. Wang, Y. Xie, L. Chen, T. Yan, Design strategies of ZnO heterojunction arrays towards effective photovoltaic applications, Batter. Energy. 1 (2022) 20210008.
[11] H.S. Das, R. Das, P.K. Nandi, S. Biring, S.K. Maity, Influence of Ga-doped transparent conducting ZnO thin film for efficiency enhancement in organic light-emitting diode applications, Appl. Phys. A. 127 (2021) 225.
[12] Y. Li, F. Yu, G. Li, M. Lu, Y. Lu, MgZnO High-Voltage Transparent Thin-Film Transistors Built on Glass, Phys. Status Solidi. 219 (2022) 2200313.
[13] L. Xue, W. Fan, Y. Yu, K. Dong, C. Liu, Y. Sun, C. Zhang, W. Chen, R. Lei, K. Rong, A novel strategy to fabricate core-sheath structure piezoelectric yarns for wearable energy harvesters, Adv. Fiber Mater. 3 (2021) 239–250.
[14] W. Chen, W. Fan, Q. Wang, X. Yu, Y. Luo, W. Wang, R. Lei, Y. Li, A nano-micro structure engendered abrasion resistant, superhydrophobic, wearable triboelectric yarn for self-powered sensing, Nano Energy 103 (2022) 107769.
[15] H.T. Hussein, M.K.A. Mohammed, R.I. Kamel, U.M. Nayef, Improved sensing performance of porous silicon photodetector with CuO nanoparticles, Chem. Pap. 75 (2021) 6257–6264.
[16] P.S. Dhanaselvam, D.S. Kumar, V.N. Ramakrishnan, K. Ramkumar, N. B. Balamurugan, Pressure sensors using si/zno heterojunction diode, SILICON 14 (2022) 4121–4127.
[17] C.A. Betty, S. Choudhury, A. Shah, Nanostructured metal oxide semiconductors and composites for reliable trace gas sensing at room temperature, Surf. Interfaces 36 (2023) 102560.
[18] A. Boublia, Z. Guezzout, N. Haddaoui, M. Badawi, A.S. Darwish, T. Lemaoui, S.E. I. Lebouachera, K.K. Yadav, M.A. Alreshidi, J.S. Algethami, M. Abbas, F. Banat, I. M. AlNashef, B.H. Jeon, Y. Benguerba, The curious case of polyaniline-graphene nanocomposites: a review on their application as exceptionally conductive and gas sensitive materials, Crit. Rev. Solid State Mater. Sci. 49 (2024) 973–997, https://doi.org/10.1080/10408436.2023.2274900.
[19] A. Boublia, Z. Guezzout, N. Haddaoui, M. Badawi, A.S. Darwish, T. Lemaoui, F. Banat, K.K. Yadav, B.H. Jeon, N. Elboughdiri, Y. Benguerba, I.M. Al Nashef, Enhancing precision in PANI/Gr nanocomposite design: robust machine learning models, outlier resilience, and molecular-input insights for superior electrical conductivity and gas sensing performance, J. Mater. Chem. A. 12 (2023) 2209–2236, https://doi.org/10.1039/d3ta06385b.
[20] R. Shwetharani, H.R. Chandan, M. Sakar, G.R. Balakrishna, K.R. Reddy, A. V. Raghu, Photocatalytic semiconductor thin films for hydrogen production and environmental applications, Int. J. Hydrogen Energy. 45 (2020) 18289–18308.
[21] S. Vyas, A short review on properties and applications of zinc oxide based thin films and devices: ZnO as a promising material for applications in electronics, optoelectronics, biomedical and sensors, Johnson Matthey, Technol. Rev. 64 (2020) 202–218.
[22] S. Pandiyaraj, M. Murali, S. Muthusamy, H. Panchal, Ultrasonically synthesized MgZnO nanoparticles for enhanced piezo-photocatalysis and MgZnO/p-Si heterojunction diode characteristics, Energy Sources Part A Recover. Util. Environ. Eff. 45 (2023) 762–776.
[23] J.C. Fan, K.M. Sreekanth, Z. Xie, S.L. Chang, K.V. Rao, p-Type ZnO materials: theory, growth, properties and devices, Prog. Mater. Sci. 58 (2013) 874–985.
[24] D. Panda, T.-Y. Tseng, One-dimensional ZnO nanostructures: fabrication, optoelectronic properties, and device applications, J. Mater. Sci. 48 (2013) 6849–6877.
[25] M.A.H. Khan, M.V. Rao, Gallium nitride (GaN) nanostructures and their gas sensing properties: a review, Sensors 20 (2020) 3889.
[26] A. Goktas, S. Modanlı, A. Tumbul, A. Kilic, Facile synthesis and characterization of ZnO, ZnO: Co, and ZnO/ZnO: Co nano rod-like homojunction thin films: role of crystallite/grain size and microstrain in photocatalytic performance, J. Alloys Compd. 893 (2022) 162334.
[27] M. Golam Azam, Preparation, characterization and photocatalytic activity of magnesium doped zinc oxide thin films, (2019).
[28] X.-L. Lu, X.-B. Guo, F.-C. Su, W.-H. Qiu, Z. Su, J. Li, W.-H. Li, Y.-P. Jiang, Z.-H. Tang, X.-G. Tang, Photoelectric characteristics of Al-doped ZnO/p-Si diode prepared by radio frequency magnetron sputtering, J. Phys. D. Appl. Phys. 55 (2022) 485101.
[29] V.L. Patil, D.S. Dalavi, S.B. Dhavale, S.A. Vanalakar, N.L. Tarwal, A.S. Kalekar, J. H. Kim, P.S. Patil, Indium doped ZnO nanorods for chemo resistive $NO_2$ gas sensors, New J. Chem. 46 (2022) 7588–7597.
[30] F. Boufelgha, R. Zellagui, M.-C. Benachour, H. Dehdouh, F. Labrèche, N. Brihi, Effect of Sn doping on the photocatalytic properties of ZnO, in, Phys. Sci. Forum, MDPI (2023) 7.
[31] P. Dumrongrojthanath, A. Phuruangrat, S. Thongtem, T. Thongtem, Photocatalysis of Cd-doped ZnO synthesized with precipitation method, Rare Met. 40 (2021) 537–546.
[32] A. Muhammed, T.G. Asere, T.F. Diriba, Photocatalytic and antimicrobial properties of ZnO and Mg-doped ZnO nanoparticles synthesized using Lupinus albus leaf extract, ACS Omega 9 (2024) 2480–2490.
[33] F. Güell, A. Galdámez-Martínez, P.R. Martínez-Alanis, A.C. Catto, L.F. da Silva, V. R. Mastelaro, G. Santana, A. Dutt, ZnO-based nanomaterials approach for photocatalytic and sensing applications: recent progress and trends, Mater. Adv. 4 (2023) 3685–3707.
[34] H. Pan, Y.P. Feng, Semiconductor nanowires and nanotubes: effects of size and surface-to-volume ratio, ACS Nano 2 (2008) 2410–2414.
[35] S.K. Nadikatla, V.B. Chintada, T.R. Gurugubelli, R. Koutavarapu, Review of recent developments in the fabrication of ZnO/CdS heterostructure photocatalysts for degradation of organic pollutants and hydrogen production, Molecules 28 (2023) 4277.
[36] A. Asadi, N. Daglioglu, T. Hasani, N. Farhadian, Construction of Mg-doped ZnO/g-C3N4@ ZIF-8 multi-component catalyst with superior catalytic performance for the degradation of illicit drug under visible light, Colloids Surf. A Physicochem. Eng. Asp. 650 (2022) 129536.
[37] I.S. Okeke, K.K. Agwu, A.A. Ubachukwu, I.G. Madiba, M. Maaza, G.M. Whyte, F. I. Ezema, Impact of particle size and surface defects on antibacterial and photocatalytic activities of undoped and Mg-doped ZnO nanoparticles, biosynthesized using one-step simple process, Vacuum 187 (2021) 110110.
[38] A.G. Oliveira, J. de Lara Andrade, M.C. Montanha, C.Y.L. Ogawa, T.K.F. de Souza Freitas, J.C.G. Moraes, F. Sato, S.M. Lima, L.H. da Cunha Andrade, A.A. W. Hechenleitner, Wastewater treatment using Mg-doped ZnO nano-semiconductors: a study of their potential use in environmental remediation, J. Photochem. Photobiol. A Chem. 407 (2021) 113078.
[39] M.R. Islam, M.G. Azam, Enhanced photocatalytic activity of Mg-doped ZnO thin films prepared by sol-gel method, Surf. Eng. 37 (2021) 775–783.
[40] K.M. Salman, M. Zikriya, R. CG, D.G. JHAA, Modulation of Band Gap by Varying Spin Coating Rotation Speed and its Effect on Structural, Optical, and Electronic Properties Of Mg-Doped Zno Thin Films for Optoelectronic Applications, Opt. Electron. Prop. Mg-Doped Zno Thin Film. Optoelectron. Appl. (n.d.).
[41] D. Sahu, N.R. Panda, B.S. Acharya, Effect of Gd doping on structure and photoluminescence properties of ZnO nanocrystals, Mater. Res. Express. 4 (2017) 114001.

[42] A. Franco Jr, H.V.S. Pessoni, Effect of Gd doping on the structural, optical band-gap, dielectric and magnetic properties of ZnO nanoparticles, Phys. B Condens. Matter. 506 (2017) 145–151.
[43] S. Vishwanathan, S. Das, Glucose-mediated one-pot hydrothermal synthesis of hollow magnesium oxide-zinc oxide (MgO-ZnO) microspheres with enhanced natural sunlight photocatalytic activity, Environ. Sci. Pollut. Res. 30 (2023) 8512–8525.
[44] Y. Wang, X. Zhao, L. Duan, F. Wang, H. Niu, W. Guo, A. Ali, Structure, luminescence and photocatalytic activity of Mg-doped ZnO nanoparticles prepared by auto combustion method, Mater. Sci. Semicond. Process. 29 (2015) 372–379.
[45] A. Ievtushenko, V. Karpyna, L. Myroniuk, D. Myroniuk, L. Petrosian, O. Olifan, O. Kolomys, V. Strelchuk, Effect of magnesium doping on the structure, optical properties and photocatalytic efficiency of ZnO nanostructures deposited by atmospheric pressure MOCVD, Chem. Phys. Lett. 857 (2024) 141720, https://doi.org/10.1016/j.cplett.2024.141720.
[46] S. Kumari, A. Kumari, K. Sharma, J. Ahmed, R. Jasrotia, A. Kandwal, N. Lakshmaiya, M. Sillanpää, R. Sharma, Enhanced photocatalytic and antimicrobial performance of divalent metal substituted nickel nanostructures for wastewater treatment and biological applications, J. Inorg. Organomet. Polym. Mater. 1–21 (2024).
[47] R.E. Adam, H. Alnoor, G. Pozina, X. Liu, M. Willander, O. Nur, Synthesis of Mg-doped ZnO NPs via a chemical low-temperature method and investigation of the efficient photocatalytic activity for the degradation of dyes under solar light, Solid State Sci. 99 (2020) 106053, https://doi.org/10.1016/j.solidstatesciences.2019.106053.
[48] G. Kasi, J. Seo, Influence of Mg doping on the structural, morphological, optical, thermal, and visible-light responsive antibacterial properties of ZnO nanoparticles synthesized via co-precipitation, Mater. Sci. Eng. C. 98 (2019) 717–725.
[49] S. Amamra, I. Kaabi, L. Arrar, A. Baghiani, M. Hamla, S.I. Aouni, I. Lakikza, A. Boublia, B. Ernst, M. Raish, Y. Benguerba, Thymus vulgaris Extract: A Green Approach to Antioxidant Efficacy, Antibacterial Action, and Corrosion Inhibition, J. Environ. Chem. Eng. (2025) 116067, https://doi.org/10.1016/j.jece.2025.116067.
[50] S. Azad, S. Chand, Synthesis and investigation of pure and doped-ZnO nanoparticles as efficient material for photocatalytic degradation of methylene blue under solar radiations, Indian J. Phys. 98 (2024) 2285–2297.
[51] J. AlYammahi, A.S. Darwish, T. Lemaoui, A. Boublia, Y. Benguerba, I. M. AlNashef, F. Banat, Molecular guide for selecting green deep eutectic solvents with high monosaccharide solubility for food applications, ACS Omega 8 (2023) 26533–26547, https://doi.org/10.1021/acsomega.3c03326.
[52] A. Boublia, T. Lemaoui, F. Abu Hatab, A.S. Darwish, F. Banat, Y. Benguerba, I. M. AlNashef, Molecular-based artificial neural network for predicting the electrical conductivity of deep eutectic solvents, J. Mol. Liq. 366 (2022) 120225, https://doi.org/10.1016/j.molliq.2022.120225.
[53] A. Boublia, T. Lemaoui, J. AlYammahi, A.S. Darwish, A. Ahmad, M. Alam, F. Banat, Y. Benguerba, I.M. AlNashef, Multitask neural network for mapping the glass transition and melting temperature space of homo- and Co-polyhydroxyalkanoates using σ profiles molecular inputs, ACS Sust. Chem. Eng. 11 (2023) 208–227, https://doi.org/10.1021/acssuschemeng.2c05225.
[54] Y. Islam Touahria, N. Chafai, O. Moumeni, A. Boublia, M. Mehri, Y. Benguerba, Synthesis, characterization, and comprehensive computational analysis of aromatic hydrazone compounds: Unveiling quantum parameters, evaluating antioxidant activity, and investigating molecular docking interactions, J. Mol. Liq. 403 (2024) 124897, https://doi.org/10.1016/j.molliq.2024.124897.
[55] A. Neni, A. Boublia, M. Bouras, K. Bentoumi, M. Albrahim, N. Elboughdiri, Y. Benguerba, Evaluating asphaltene dispersion with choline chloride or menthol based deep eutectic solvents: a COSMO-RS analysis, J. Mol. Liq. 407 (2024) 125272, https://doi.org/10.1016/j.molliq.2024.125272.
[56] B.M. Popović, D. Uka, O. Alioui, R. Ždero Pavlović, Y. Benguerba, Experimental and COSMO-RS theoretical exploration of rutin formulations in natural deep eutectic solvents: Solubility, stability, antioxidant activity, and bioaccessibility, J. Mol. Liq. 359 (2022), https://doi.org/10.1016/j.molliq.2022.119266.
[57] D. Uka, B. Blagojević, O. Alioui, A. Boublia, N. Elboughdiri, Y. Benguerba, T. Jurić, B.M. Popović, An innovative and environmentally friendly approach for resveratrol solubilization and bioaccessibility enhancement by using natural deep eutectic solvents, J. Mol. Liq. 391 (2023) 123411, https://doi.org/10.1016/j.molliq.2023.123411.
[58] T. Lemaoui, A.S. Darwish, G. Almustafa, A. Boublia, P.R. Sarika, N.A. Jabbar, T. Ibrahim, P. Nancarrow, K.K. Yadav, A.M. Fallatah, M. Abbas, J.S. Algethami, Y. Benguerba, B.H. Jeon, F. Banat, I.M. AlNashef, Machine learning approach to map the thermal conductivity of over 2,000 neoteric solvents for green energy storage applications, Energy Storage Mater. 59 (2023) 102795, https://doi.org/10.1016/j.ensm.2023.102795.
[59] T. Lemaoui, A. Boublia, A.S. Darwish, M. Alam, S. Park, B.H. Jeon, F. Banat, Y. Benguerba, I.M. Alnashef, Predicting the surface tension of deep eutectic solvents using artificial neural networks, ACS Omega 7 (2022) 32194–32207, https://doi.org/10.1021/acsomega.2c03458.
[60] A. Mouffok, D. Bellouche, I. Debbous, A. Anane, Y. Khoualdia, A. Boublia, A. S. Darwish, T. Lemaoui, Y. Benguerba, Synergy of garlic extract and deep eutectic solvents as promising natural Antibiotics: experimental and COSMO-RS, J. Mol. Liq. 375 (2023) 121321, https://doi.org/10.1016/j.molliq.2023.121321.
[61] A. Boublia, N. Elboughdiri, J. Georgin, K.K. Yadav, D. Ghernaout, D.S.P. Franco, M. Benaissa, A.A.M. Salih, M. Albrahim, M.S. Hamdy, Y. Benguerba, Zinc chloride-assisted activation of açaí biomass for herbicide removal: Insights from adsorption and molecular modeling, Process Saf. Environ. Prot. 188 (2024) 385–397, https://doi.org/10.1016/j.psep.2024.05.085.
[62] A.E. Zemouri, E. Bentouhami, H. Zaghouane-Boudiaf, Y.I. Touahria, G. Bellil, A. Boublia, N. Daas, T. Dintzer, N. Chafai, M. Albrahim, N. Elboughdiri, Y. Benguerba, Efficient wastewater decontamination using magnetic bentonite-alginate beads: a comprehensive study of adsorption dynamics, regeneration, and molecular interactions, J. Environ. Chem. Eng. 12 (2024) 113000, https://doi.org/10.1016/j.jece.2024.113000.
[63] K. Rouibah, H. Ferkous, M. Abdessalam-Hassan, B.L. Mossab, A. Boublia, C. Pierlot, A. Abdennouri, I. Avramova, M. Alam, Y. Benguerba, A. Erto, Exploring the efficiency of algerian kaolinite clay in the adsorption of Cr(III) from aqueous solutions: experimental and computational insights, Molecules 29 (2024), https://doi.org/10.3390/molecules29092135.
[64] K.A. Moltved, K.P. Kepp, Performance of density functional theory for transition metal oxygen bonds, ChemPhysChem 20 (2019) 3210–3220, https://doi.org/10.1002/cphc.201900862.
[65] C. Boulechfar, H. Ferkous, A. Delimi, M. Berredjem, A. Kahlouche, A. Madaci, S. Djellali, S. Boufas, A. Djedouani, A. Errachid, A. Ali Khan, A. Boublia, T. Lemaoui, Y. Benguerba, Corrosion inhibition of Schiff base and their metal complexes with [Mn (II), Co (II) and Zn (II)]: experimental and quantum chemical studies, J. Mol. Liq. 378 (2023) 121637. DOi: 10.1016/j.molliq.2023.121637.
[66] C. Boulechfar, H. Ferkous, A. Delimi, A. Djedouani, A. Kahlouche, A. Boublia, A. S. Darwish, T. Lemaoui, R. Verma, Y. Benguerba, Schiff bases and their metal Complexes: a review on the history, synthesis, and applications, Inorg. Chem. Commun. 150 (2023) 110451, https://doi.org/10.1016/j.inoche.2023.110451.
[67] A. Boublia, Z. Guezzout, N. Haddaoui, M. Badawi, I. Lakikza, I. Belkhettab, O. Moumeni, S.I. Aouni, M. Alam, Y. Benguerba, Comprehensive investigation of multifunctional polyaniline/reduced graphene oxide nanocomposites synthesized from deep eutectic solvents: experimental, RSM, ANN and computational studies, Mater. Adv. (2024), https://doi.org/10.1039/d4ma00231h.
[68] I. Akkari, Z. Graba, N. Bezzi, M.M. Kaci, F.A. Merzeg, N. Bait, A. Ferhati, G. L. Dotto, Y. Benguerba, Effective removal of cationic dye on activated carbon made from cactus fruit peels: a combined experimental and theoretical study, Environ. Sci. Pollut. Res. 30 (2023) 3027–3044, https://doi.org/10.1007/s11356-022-22402-4.
[69] C. Boulechfar, H. Ferkous, S. Djellali, M.A. Amin, S. Boufas, A. Djedouani, A. Delimi, Y. Ben Amor, K. Kumar Yadav, B.H. Jeon, Y. Benguerba, DFT/molecular scale, MD simulation and assessment of the eco-friendly anti-corrosion performance of a novel Schiff base on XC38 carbon steel in acidic medium, J. Mol. Liq. 344 (2021) 117874, https://doi.org/10.1016/j.molliq.2021.117874.
[70] Z. Jebali, H. Ferkous, M. Zerroug, A. Boublia, A. Delimi, A. Bouzid, H. Majdoub, B. Ernst, N. Elboughdiri, Y. Benguerba, Unveiling the potent corrosion-inhibiting power of Ammophila arenaria aqueous extract for mild steel in acidic environments: An integrated experimental and computational study, J. Environ. Chem. Eng. 12 (2024) 112374, https://doi.org/10.1016/j.jece.2024.112374.
[71] E.R. Johnson, S. Keinan, P. Mori-Sánchez, J. Contreras-García, A.J. Cohen, W. Yang, Revealing noncovalent interactions, J. Am. Chem. Soc. 132 (2010) 6498–6506, https://doi.org/10.1021/ja100936w.
[72] I. Lakikza, H. Ghodbane, M.L. Chelaghmia, A. Boublia, S.I. Aouni, I. Belkhettab, H. Ferkous, A. Erto, A.S. Bentali, Y. Benguerba, Unraveling the corrosion inhibition mechanisms of algerian dryopteris filix mas leaf extract on A210C carbon steel in 1M HCl: comprehensive insights from electrochemical, morphological, XPS, and theoretical analyses, Mater. Today Commun. (2024) 111262, https://doi.org/10.1016/j.mtcomm.2024.111262.
[73] T. Lu, F. Chen, Multiwfn: a multifunctional wavefunction analyzer, J. Comput. Chem. 33 (2012) 580–592, https://doi.org/10.1002/jcc.22885.
[74] T. Yasmin, A. Mahmood, R.M. Sarfraz, U. Rehman, A. Boublia, A.M. Alkahtani, G. S. Albakri, H. Ijaz, S. Ahmed, B. Harron, M. Albrahim, N. Elboughdiri, K.K. Yadav, Y. Benguerba, Mimosa/quince seed mucilage–co-poly (methacrylate) hydrogels for controlled delivery of capecitabine: simulation studies, characterization, and toxicological evaluation, Int. J. Biol. Macromol. 275 (2024) 133468, https://doi.org/10.1016/j.ijbiomac.2024.133468.
[75] T. Yasmin, A. Mahmood, M. Farooq, R.M. Sarfraz, A. Boublia, U. Rehman, M. U. Ashraf, J.K. Bhutto, B. Ernst, M. Albrahim, N. Elboughdiri, K.K. Yadav, M. A. Alreshidi, H. Ijaz, Y. Benguerba, Development and evaluation of a pH-responsive Mimosa pudica seed mucilage/β- cyclodextrin-co-poly(methacrylate) hydrogel for controlled drug delivery: in vitro and in vivo assessment, Int. J. Biol. Macromol. 268 (2024) 131832, https://doi.org/10.1016/j.ijbiomac.2024.131832.
[76] T. Yasmin, A. Mahmood, M. Farooq, U. Rehman, R.M. Sarfraz, H. Ijaz, M. R. Akram, A. Boublia, M.M. Salem Bekhit, B. Ernst, Y. Benguerba, Quince seed mucilage/β-cyclodextrin/Mmt-Na+-co-poly (methacrylate) based pH-sensitive polymeric carriers for controlled delivery of Capecitabine, Int. J. Biol. Macromol. 253 (2023) 127032, https://doi.org/10.1016/j.ijbiomac.2023.127032.
[77] C. Williams, T. Kelley, Gnuplot 4.5: an interactive plotting program., URL Http//Www, Gnuplot. Info. 56 (2011). http://www.gnuplot.info/.
[78] W. Humphrey, A. Dalke, K. Schulten, VMD: Visual molecular dynamics, J. Mol. Graph. 14 (1996) 33–38, https://doi.org/10.1016/0263-7855(96)00018-5.
[79] D. Bousba, C. Sobhi, E. Zouaoui, K. Rouibah, A. Boublia, H. Ferkous, A. Haddad, A. Gouasmia, I. Avramova, Z. Mohammed, V.I. Parvulescu, K.K. Yadav, M. Hasan, M.M.S. Cabral-Pinto, N. Elboughdiri, Y. Benguerba, Efficient biodiesel production from recycled cooking oil using a NaOH/CoFe2O4 magnetic nano-catalyst: synthesis, characterization, and process enhancement for sustainability, Energy Convers, Manag 300 (2024) 118021, https://doi.org/10.1016/j.enconman.2023.118021.

[80] F.K. Shan, B.I. Kim, G.X. Liu, Z.F. Liu, J.Y. Sohn, W.J. Lee, B.C. Shin, Y.S. Yu, Blueshift of near band edge emission in Mg-doped ZnO thin films and aging, J. Appl. Phys. 95 (2004) 4772–4776.

[81] M. Dehimi, T. Touam, A. Chelouche, F. Boudjouan, D. Djouadi, J. Solard, A. Fischer, A. Boudrioua, A. Doghmane, Effects of low Ag doping on physical and optical waveguide properties of highly oriented sol-gel ZnO thin films, Adv. Condens. Matter Phys. 2015 (2015) 740208.

[82] L. Umaralikhan, M.J.M. Jaffar, Green synthesis of ZnO and Mg-doped ZnO nanoparticles, and its optical properties, J. Mater. Sci. Mater. Electron. 28 (2017) 7677–7685, https://doi.org/10.1007/s10854-017-6461-1.

[83] V. Etacheri, R. Roshan, V. Kumar, Mg-doped ZnO nanoparticles for efficient sunlight-driven photocatalysis, ACS Appl. Mater. Interfaces. 4 (2012) 2717–2725.

[84] O. Dobrozhan, O. Diachenko, M. Kolesnyk, A. Stepanenko, S. Vorobiov, P. Baláž, S. Plotnikov, A. Opanasyuk, Morphological, structural and optical properties of Mg-doped ZnO nanocrystals synthesized using polyol process, Mater. Sci. Semicond. Process. 102 (2019) 104595.

[85] G. Kasi, K. Viswanathan, J. Seo, Effect of annealing temperature on the morphology and antibacterial activity of Mg-doped zinc oxide nanorods, Ceram. Int. 45 (2019) 3230–3238, https://doi.org/10.1016/j.ceramint.2018.10.226.

[86] E.Y. Shaba, J.O. Jacob, J.O. Tijani, M.A.T. Suleiman, A critical review of synthesis parameters affecting the properties of zinc oxide nanoparticle and its application in wastewater treatment, Appl. Water Sci. 11 (2021) 48.

[87] P.S. Shewale, Y.S. Yu, Structural, surface morphological and UV photodetection properties of pulsed laser deposited Mg-doped ZnO nanorods: effect of growth time, J. Alloys Compd. 654 (2016) 79–86.

[88] R.L. Manjunatha, K.V. Usharani, D. Naik, Synthesis and characterization of ZnO nanoparticles: a review, J. Pharmacogn. Phytochem. 8 (2019) 1095–1101.

[89] M. Rouchdi, E. Salmani, B. Fares, N. Hassanain, A. Mzerd, Synthesis and characteristics of Mg-doped ZnO thin films: experimental and ab-initio study, Results Phys. 7 (2017) 620–627.

[90] N.A. Hammed, A.A. Aziz, A.I. Usman, M.A. Qaeed, The sonochemical synthesis of vertically aligned ZnO nanorods and their UV photodetection properties: effect of ZnO buffer layer, Ultrason. Sonochem. 50 (2019) 172–181.

[91] S.F. Shayesteh, A.A. Dizgah, Effect of doping and annealing on the physical properties of ZnO: Mg nanoparticles, Pramana 81 (2013) 319–330.

[92] O. Kalu, M.R. Correia, A. Cantarero, H.A. Martinez-Rodriguez, J.A. Duarte-Moller, A. Reyes-Rojas, Enhanced optical properties of Cd–Mg-co-doped ZnO nanoparticles induced by low crystal structure distortion, J. Phys. Chem. Solids. 146 (2020) 109611.

[93] X. Yu, X. Yu, M. Yan, T. Weng, L. Chen, Y. Zhou, J. Wei, Lowering oxygen vacancies of ZnO nanorods via Mg-doping and their effect on polymeric diode behavior, Sens. Actuat. A Phys. 312 (2020) 112163.

[94] Y. Chen, Q. Zhang, C. Flach, R. Mendelsohn, E. Galoppini, P.I. Reyes, K. Yang, R. Li, G. Li, Y. Lu, Functionalization of MgZnO nanorod films and characterization by FTIR microscopic imaging, Anal. Bioanal. Chem. 409 (2017) 6379–6386.

[95] G. Lavanya, T. Suvarna, C.P. Vardhani, Structural and Optical Properties of (MgZnO/rGO) Nanocomposites, J. Chem. Lett. 4 (2023) 136–147.

[96] A.E. Jimenez-Gonzalez, J.A.S. Urueta, R. Suarez-Parra, Optical and electrical characteristics of aluminum-doped ZnO thin films prepared by sol-gel technique, J. Cryst. Growth. 192 (1998) 430–438.

[97] S.C. Pillai, J.M. Kelly, D.E. McCormack, P. O'Brien, R. Ramesh, The effect of processing conditions on varistors prepared from nanocrystalline ZnO, J. Mater. Chem. 13 (2003) 2586–2590.

[98] F. Mohandes, F. Davar, M. Salavati-Niasari, Magnesium oxide nanocrystals via thermal decomposition of magnesium oxalate, J. Phys. Chem. Solids. 71 (2010) 1623–1628.

[99] X.S. Wang, Z.C. Wu, J.F. Webb, Z.G. Liu, Ferroelectric and dielectric properties of Li-doped ZnO thin films prepared by pulsed laser deposition, Appl. Phys. A Mater. Sci. Process. 77 (2003) 561–565, https://doi.org/10.1007/s00339-002-1497-2.

[100] A.N. Mallika, A.R. Reddy, K.S. Babu, C. Sujatha, K.V. Reddy, Structural and photoluminescence properties of Mg substituted ZnO nanoparticles, Opt. Mater. (amst) 36 (2014) 879–884.

[101] S.S. Wagh, C.V. Jagtap, V.S. Kadam, S.F. Shaikh, M. Ubaidullah, P. Bidhan, D. B. Salunkhe, R.S. Patil, Silver doped ZnO nanoparticles synthesized for photocatalysis application, ES Energy Environ. 17 (2022) 94–105.

[102] H. Naseer, N. Al-Zaqri, T. Iqbal, M. Yousaf, S. Afsheen, M.S. Sultan, I. Warad, M. Farooq, A. Masood, Investigation of Mg-doped ZnO nanoparticles decorated with Ag for efficient photocatalytic degradation, J. Inorg. Organomet. Polym. Mater. 33 (2023) 2790–2802.

[103] K. Pradeev Raj, K. Sadaiyandi, A. Kennedy, S. Sagadevan, Z.Z. Chowdhury, M. R. Bin Johan, F.A. Aziz, R.F. Rafique, R. Thamiz Selvi, R. Rathina Bala, Influence of Mg doping on ZnO nanoparticles for enhanced photocatalytic evaluation and antibacterial analysis, Nanoscale Res. Lett. 13 (2018) 1–13.

[104] S.M. Nagasundari, K. Muthu, K. Kaviyarasu, D.A. Al Farraj, R.M. Alkufeidy, Current trends of Silver doped Zinc oxide nanowires photocatalytic degradation for energy and environmental application, Surf. Interfaces 23 (2021) 100931.

[105] Y. Nosaka, A.Y. Nosaka, Generation and detection of reactive oxygen species in photocatalysis, Chem. Rev. 117 (2017) 11302–11336.

[106] H. Agbe, N. Raza, D. Dodoo-Arhin, R.V. Kumar, K.-H. Kim, A simple sensing of hazardous photo-induced superoxide anion radicals using a molecular probe in ZnO-Nanoparticles aqueous medium, Environ. Res. 176 (2019) 108424.

[107] X.X. Yu, Y. Wu, B. Dong, Z.F. Dong, X. Yang, Enhanced solar light photocatalytic properties of ZnO nanocrystals by Mg-doping via polyacrylamide polymer method, J. Photochem. Photobiol. A Chem. 356 (2018) 681–688.

[108] G. Yi, X. Li, Y. Yuan, Y. Zhang, Redox-active Zn/ZnO duo generating superoxide ( O 2−) and $H_2O_2$ under all conditions for environmental sanitation, Environ. Sci. Nano 6 (2019) 68–74.

[109] M. Kuru, The effect of thickness on photocatalytic performance in MgZnO thin films, Sak. Univ. J. Sci. 24 (2020) 586–595, https://doi.org/10.16984/saufenbilder.645104.

[110] S.I. Aouni, H. Ghodbane, S. Merouani, I. Lakikza, A. Boublia, K.K. Yadav, C. Djelloul, G.S. Albakri, N. Elboughdiri, Y. Benguerba, Removal enhancement of persistent basic fuchsin dye from wastewater using an eco-friendly, cost-effective Fenton process with sodium percarbonate and waste iron catalyst, Environ. Sci. Pollut. Res. 31 (2024) 43673–43686, https://doi.org/10.1007/s11356-024-33845-2.

[111] M.G. Yazdi, M. Ivanic, A. Mohamed, A. Uheida, Surface modified composite nanofibers for the removal of indigo carmine dye from polluted water, RSC Adv. 8 (2018) 24588–24598.

[112] P.T. Juchen, H.H. Piffer, M.T. Veit, G. da Cunha Gonçalves, S.M. Palácio, J. C. Zanette, Biosorption of reactive blue BF-5G dye by malt bagasse: kinetic and equilibrium studies, J. Environ. Chem. Eng. 6 (2018) 7111–7118.

[113] T.T. Ali, K. Narasimha Rao, I.P. Parkin, C.J. Carmalt, S. Sathasivam, S.N. Basahel, S.M. Bawaked, S.A. Al-Thabaiti, Effect of pretreatment temperature on the photocatalytic activity of microwave irradiated porous nanocrystalline ZnO, New J. Chem. 39 (2015) 321–332.

[114] F.M. Omar, H.A. Aziz, S. Stoll, Aggregation and disaggregation of ZnO nanoparticles: influence of pH and adsorption of Suwannee River humic acid, Sci. Total Environ. 468 (2014) 195–201.

[115] A.S. Bhosale, K.K. Abitkar, P.S. Sadalage, K.D. Pawar, K.M. Garadkar, Photocatalytic and antibacterial activities of ZnO nanoparticles synthesized by chemical method, J. Mater. Sci. Mater. Electron. 32 (2021) 20510–20524.

[116] M. Kuru, H. Narsat, The effect of heat treatment temperature and Mg doping on structural and photocatalytic activity of ZnO thin films fabricated by RF magnetron co-sputtering technique, J. Mater. Sci. Mater. Electron. 30 (2019) 18484–18495.

[117] R. Bomila, S. Suresh, S. Srinivasan, Synthesis, characterization and comparative studies of dual doped ZnO nanoparticles for photocatalytic applications, J. Mater. Sci. Mater. Electron. 30 (2019) 582–592.

[118] L.A. Chanu, W.J. Singh, K.J. Singh, K.N. Devi, Effect of operational parameters on the photocatalytic degradation of Methylene blue dye solution using manganese doped ZnO nanoparticles, Results Phys. 12 (2019) 1230–1237.

[119] A.N. Kadam, T.G. Kim, D.S. Shin, K.M. Garadkar, J. Park, Morphological evolution of Cu doped ZnO for enhancement of photocatalytic activity, J. Alloys Compd. 710 (2017) 102–113.

[120] I. Lakikza, Y. Benguerba, A. Boublia, S.I. Aouni, H. Lahbib, H. Ferkous, H. Ghodbane, Y. Benamor, A. Sami Bentalib, B. Ernst, Comprehensive evaluation of Alysicarpus compactum extract as a natural corrosion inhibitor for St37 carbon steel in acidic media, J. Ind. Eng. Chem. (2024), https://doi.org/10.1016/j.jiec.2024.12.010.

[121] F.L. Theiss, G.A. Ayoko, R.L. Frost, Synthesis of layered double hydroxides containing Mg2+, Zn2+, Ca2+, and Al3+ layer cations by co-precipitation methods—a review, Appl. Surf. Sci. 383 (2016) 200–213.

[122] M. Samadi, M. Zirak, A. Naseri, E. Khorashadizade, A.Z. Moshfegh, Recent progress on doped ZnO nanostructures for visible-light photocatalysis, Thin Solid Films 605 (2016) 2–19, https://doi.org/10.1016/j.tsf.2015.12.064.

[123] A. Moulahi, Efficient photocatalytic performance of Mg doping ZnO for the photodegradation of the rhodamine B, Inorg. Chem. Commun. 133 (2021) 108906, https://doi.org/10.1016/j.inoche.2021.108906.

[124] M. Ahmad, W. Rehman, M.M. Khan, M.T. Qureshi, A. Gul, S. Haq, R. Ullah, A. Rab, F. Menaa, Phytogenic fabrication of ZnO and gold decorated ZnO nanoparticles for photocatalytic degradation of Rhodamine B, J. Environ. Chem. Eng. 9 (2021) 104725, https://doi.org/10.1016/j.jece.2020.104725.

[125] T.K. Pathak, R.E. Kroon, H.C. Swart, Photocatalytic and biological applications of Ag and Au doped ZnO nanomaterial synthesized by combustion, Vacuum 157 (2018) 508–513, https://doi.org/10.1016/j.vacuum.2018.09.020.

[126] M. Mittal, M. Sharma, O.P. Pandey, UV-Visible light induced photocatalytic studies of Cu doped ZnO nanoparticles prepared by co-precipitation method, Sol. Energy. 110 (2014) 386–397, https://doi.org/10.1016/j.solener.2014.09.026.

[127] K. Qi, X. Xing, A. Zada, M. Li, Q. Wang, S. Liu, H. Lin, G. Wang, Transition metal doped ZnO nanoparticles with enhanced photocatalytic and antibacterial performances: Experimental and DFT studies, Ceram. Int. 46 (2020) 1494–1502, https://doi.org/10.1016/j.ceramint.2019.09.116.

[128] K. Pradeev Raj, K. Sadaiyandi, A. Kennedy, S. Sagadevan, Photocatalytic and antibacterial studies of indium-doped ZnO nanoparticles synthesized by co-precipitation technique, J. Mater. Sci. Mater. Electron. 28 (2017) 19025–19037, https://doi.org/10.1007/s10854-017-7857-7.

[129] P.M. Perillo, M.N. Atia, Solar-assisted photodegradation of methyl orange using Cu-doped ZnO nanorods, Mater. Today Commun. 17 (2018) 252–258, https://doi.org/10.1016/j.mtcomm.2018.09.010.

[130] S. Jagadhesan, N. Senthilkumar, V. Senthilnathan, T.S. Senthil, Sb doped ZnO nanostructures prepared via co-precipitation approach for the enhancement of MB dye degradation, Mater. Res. Express. 5 (2018) 25040.

[131] O. Długosz, K. Szostak, M. Banach, Photocatalytic properties of zirconium oxide–zinc oxide nanoparticles synthesized using microwave irradiation, Appl. Nanosci. 10 (2020) 941–954, https://doi.org/10.1007/s13204-019-01158-3.

[132] R. Kumar, H.S. Dosanjh, A mini-review on rare earth metal doped ZnO nanomaterials for photocatalytic remediation of wastewater, in: J. Phys. Conf. Ser., IOP Publishing, 2022, p. 12139.

[133] L. Aroui, S. Madani, I. Bousnoubra, A. Boublia, I. Lakikza, S.I. Aouni, L. Abdelouahed, B. Ernst, M. Alam, Y. Benguerba, Enhanced degradation of crystal violet using PANI-ZnO nanocomposites: electro-oxidation and photocatalysis studies, J. Mol. Liq. 412 (2024) 125818, https://doi.org/10.1016/j.molliq.2024.125818.
[134] N. Elboughdiri, I. Lakikza, A. Boublia, S.I. Aouni, N. El Houda Hammoudi, J. Georgin, D.S.P. Franco, H. Ferkous, D. Ghernaout, Y. Benguerba, Application of statistical physical, DFT computation and molecular dynamics simulation for enhanced removal of crystal violet and basic fuchsin dyes utilizing biosorbent derived from residual watermelon seeds (Citrullus lanatus), Process Saf. Environ. Prot. 186 (2024) 995–1010, https://doi.org/10.1016/j.psep.2024.03.093.
[135] H. Ferkous, S. Guezane-Lakoud, A. Sedik, A. Boublia, A. Delimi, A. Kahlouche, C. Boulechfar, Y. Dilgin, K.S.A. Halim, M. Albrahim, Y. Benguerba, Tailored α-hydroxyphosphonate derivatives: Green synthesis, spectroscopic characterization, DFT analysis, and high-efficiency corrosion protection for copper in acidic media, Sustain. Mater. Technol. (2025) e01282, https://doi.org/10.1016/j.susmat.2025.e01282.
[136] J.O. de Brito Lira, H.G. Riella, N. Padoin, C. Soares, An overview of photoreactors and computational modeling for the intensification of photocatalytic processes in the gas-phase: State-of-art, J. Environ. Chem. Eng. 9 (2021) 105068.
[137] F.T. Geldasa, M.A. Kebede, M.W. Shura, F.G. Hone, Experimental and computational study of metal oxide nanoparticles for the photocatalytic degradation of organic pollutants: a review, RSC Adv. 13 (2023) 18404–18442.
[138] S. Brioua, A. Delimi, H. Ferkous, S. Boukerche, H. Allal, A. Boublia, A. Djedouani, M. Berredjem, A. Kahlouche, K.O. Rachedi, A. Abdennouri, M. Alam, B. Ernst, Y. Benguerba, Enhancing corrosion resistance of XC38 steel using sulfur and nitrogen-containing phenyl thiosemicarbazone: a comprehensive experimental and computational analysis, J. Taiwan Inst. Chem. Eng. 165 (2024) 105718, https://doi.org/10.1016/j.jtice.2024.105718.
[139] N. Benachour, A. Delimi, H. Allal, A. Boublia, A. Sedik, H. Ferkous, A. Djedouani, S. Brioua, C. Boulechfar, H. Benzouid, A. Houssou, A. Oral, B. Ernst, M. Alam, Y. Benguerba, 3,4-Dimethoxy phenyl thiosemicarbazone as an effective corrosion inhibitor of copper under acidic solution: comprehensive experimental, characterization and theoretical investigations, RSC Adv. 14 (2024) 12533–12555, https://doi.org/10.1039/d3ra08629a.
[140] I. Kaabi, S. Amamra, T. Douadi, M. Al-Noaimi, N. Chafai, A. Boublia, M. Albrahim, N. Elboughdiri, Y. Benguerba, Unveiling the dual role of a novel azomethine: Corrosion inhibition and antioxidant potency – a multifaceted study integrating experimental and theoretical approaches, J. Taiwan Inst. Chem. Eng. 161 (2024) 105535, https://doi.org/10.1016/j.jtice.2024.105535.
[141] N. Mouats, S. Djellali, H. Ferkous, A. Sedik, A. Delimi, A. Boublia, K.O. Rachedi, M. Berredjem, A. Çukurovali, M. Alam, B. Ernsti, Y. Benguerba, Comprehensive Investigation of the Adsorption, Corrosion Inhibitory Properties, and Quantum Calculations for 2-(2,4,5-trimethoxybenzylidene) hydrazine carbothioamide in mitigating corrosion of XC38 carbon steel under HCl environment, ACS Omega 9 (2024) 27945–27962, https://doi.org/10.1021/acsomega.3c10240.
[142] N. Ramdane, Z. Marsa, A. Delimi, A. Sedik, A. Boublia, G.S. Albakri, M. Abbas, K. Kumar Yadav, M. Gabsi, A. Djedouani, K.O. Rachedi, L. Toukal, H. Benzouid, M. Berredjem, H. Ferkous, Y. Benguerba, Synergistic shielding of copper from nitric acid corrosion: unveiling the mechanisms through electrochemical, characterization, and computational insights with 2-Hydroxybenzaldehyde oxime, Inorg. Chem. Commun. 165 (2024) 112479, https://doi.org/10.1016/j.inoche.2024.112479.
[143] H. Ferkous, A. Sedik, A. Delimi, R. Redjemia, K. Abdesalem, C. Boulechfar, A. Abdennouri, A. Madaci, M. Berredjem, A. Boublia, M. Sajid Ali, B.H. Jeon, K. Kumar Yadav, Y. Benguerba, A comparative study of novel synthesized sulfamide compounds: electrochemical, morphological, XPS, and theoretical investigations on copper corrosion inhibition in 1.0 M HCl, J. Mol. Liq. 394 (2024) 123781, https://doi.org/10.1016/j.molliq.2023.123781.
[144] N. Elboughdiri, H. Ferkous, K. Rouibah, A. Boublia, A. Delimi, K.K. Yadav, A. Erto, D. Ghernaout, A.A.M. Salih, M. Benaissa, Y. Benguerba, Comprehensive investigation of Cu2+ adsorption from wastewater using olive-waste-derived adsorbents: experimental and molecular insights, Int. J. Mol. Sci. 25 (2024), https://doi.org/10.3390/ijms25021028.
[145] I. Lakikza, H. Ghodbane, A. Boublia, S.I. Aouni, A. Zouaoui, K.S.A.A. Al-Qasim, M. Albrahim, Y. Benguerba, Unlocking the power of Dryopteris filix mas extract: a green solution for corrosion inhibition in A210Gr carbon steel in acidified 3% wt. NaCl environment, J. Mol. Liq. 414 (2024) 126219, https://doi.org/10.1016/j.molliq.2024.126219.
[146] P.P. Selvam, V. Rathinam, A. Arunraj, A.B. Ali Baig, M. Govindhan, Synthesis effect of Mg-doped ZnO nanoparticles for visible light photocatalysis, Ionics (Kiel) 29 (2023) 3723–3729.
[147] S. Ahmad, K. Sohail, L. Chen, H. Xu, H.U. Din, Z. Zhou, Type-II van der Waals heterostructures of GeC, ZnO and Al2SO monolayers for promising optoelectronic and photocatalytic applications, Int. J. Hydrogen Energy. 48 (2023) 25354–25365, https://doi.org/10.1016/j.ijhydene.2023.03.268.
[148] K. Jia, G. Liu, D.-N. Lang, S.-F. Chen, C. Yang, R.-L. Wu, W. Wang, J.-D. Wang, Degradation of tetracycline by visible light over ZnO nanophotocatalyst, J. Taiwan Inst. Chem. Eng. 136 (2022) 104422, https://doi.org/10.1016/j.jtice.2022.104422.

**Farida Khammar** is an assistant professor in Mechanical Engineering at the University of Mohamed Chérif Messaadia, Souk Ahras, Algeria. She teaches Metrology, Sensors and Instrumentation, and Professional Projects. Her research interests include renewable energy, sustainable development, nonlinear optics, and nanomaterials. Dr. Khammar is also a member of the Laboratory of Research on Electromechanical and Dependability, collaborating on advanced research projects. Her work contributes to advancements in mechanical engineering and sustainable technologies.

**Said Boukerche** is a faculty member in the Department of Material Sciences at the University of Mohamed Chérif Messaadia, Souk Ahras, Algeria, and is affiliated with the Laboratory of Surface Engineering at the University of Badji Mokhtar, Annaba. His research focuses on the synthesis and characterization of novel materials, corrosion inhibition, and biosorption techniques for the removal of industrial dyes, heavy metals, and pharmaceuticals. He is also actively involved in exploring the bioactivity of medicinal plants. Dr. Boukerche has published extensively on electrochemical behavior, corrosion inhibitors, and bio-ceramic coatings. His work contributes to advancements in material protection, environmental remediation, and sustainable technologies.

**Selma Djaber** is a researcher in Analytical Chemistry, earning her Ph.D. from the University Mohamed-Cherif Messaadia, Souk Ahras, in 2024. Her work focuses on heavy metal extraction and environmental remediation. She has published in reputable journals such as Chemical Engineering and Processing-Process Intensification and Applied Sciences. Dr. Djaber has presented her research at international and national seminars and supervised six Master's students. She also lectures at Mohamed-Cherif Messaadia University. Her research contributes to advancing sustainable environmental solutions through innovative analytical techniques.

**Abir Boublia** is a postdoctoral researcher at the University of Lorraine. She earned her Ph.D. in Polymer Engineering in 2024 from Ferhat Abbas University, Algeria, receiving the Best Ph.D. Student Award (first place) in Algeria. Her research focuses on artificial intelligence, machine learning, and computational modeling, including Density Functional Theory (DFT) and molecular dynamics, applied to diverse materials. Dr. Boublia has published extensively in peer-reviewed journals and presented at international conferences. Her work advances computational methods in material science, driving innovation in functional materials through the integration of AI and advanced simulations.

**Abdessalam Messabhia** is a State Engineer in University Laboratories at the Department of Material Sciences, Faculty of Science and Technology, University Mohamed Chérif Messaadia, Souk Ahras, Algeria. His role involves supporting research and educational activities within the department, contributing to the advancement of material sciences.

**Amel Gharbi** is a senior researcher at the Industrial Technologies Research Center (CRTI) and member of the foundry research laboratory at the Badji Mokhtar University in Annaba, she specializes in elaboration and characterization of materials. The research she has carried out throughout her career has focused on the development and characterization of ferrous and non-ferrous alloys. She is currently involved in a project to develop zinc-based alloys for the biomedical sector.

**Hana Ferkous** is a Professor in the Department of Technology at 20 Août 1955 Skikda University, Algeria. She earned her Ph. D. in Electrochemistry-Corrosion from Badji Mokhtar Annaba University in 2010. Her research focuses on cathodic protection in marine environments, Schiff Base metal complexes, and material protection using inhibitors. With over 23 years of research experience, Dr. Ferkous has supervised multiple Ph.D. students and published extensively, including book chapters and conference presentations. Her work significantly contributes to advancements in electrochemistry and corrosion protection.

**Cristian Vacacela Gomez** holds a Bachelor's degree in Biophysics from the Escuela Superior Politécnica de Chimborazo (Ecuador), obtained in 2013, and a Ph.D. in Physics and Quantum Technologies from the University of Calabria (Italy), earned in 2017. In 2012, he served as a visiting researcher at INTEMA (Instituto de Investigaciones en Ciencia y Tecnología de Materiales) in Argentina. Currently, Dr. Vacacela Gomez holds a postdoctoral position at the Laboratori Nazionali di Frascati - Istituto Nazionale di Fisica Nucleare (LNF - INFN) and is also a Research Associate at the Department of Physics at the University of Calabria. His research focuses on the synthesis, characterization, and modeling of nanoscale materials.

**Stefano Bellucci** is a distinguished physicist specializing in theoretical physics, nanotechnology, and condensed matter. He earned his Laurea in Physics (summa cum laude) from Sapienza University of Rome and a Ph.D. in Elementary Particle Physics from SISSA, Trieste. His career includes research positions at Brandeis University, MIT, and the University of California. As Senior Research Staff at INFN Frascati, he led key projects in nanotechnology and applied physics. Dr. Bellucci has published over 900 papers with 16,300 citations and an h-index of 59. He is the Editor-in-Chief of several scientific journals and ranks among Italy's top scientists in Material and Nano Sciences. His work bridges fundamental physics with biomedical and technological applications.

**Malik Albrahim** is an assistant professor and the head of the Chemical Engineering Department at the University of Hail. He earned his Bachelor's degree in Chemical Engineering from the University of Hail in 2013, followed by a Master's degree from the University of South Florida in 2017. He then completed his Ph.D. in Chemical Engineering at Virginia Tech in 2023. His research focuses on the synthesis and characterization of advanced materials and catalysis for environmental and energy applications.

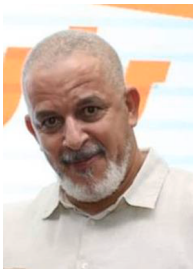

**YacineBenguerba** is a Professor in Chemical Engineering at Ferhat Abbas University, Sétif, Algeria. In 2024, he received the Best Research Professor Award (second place) in Algeria and was listed among the Top 2% Scientists Worldwide by Elsevier and Stanford University. His research focuses on deep eutectic solvents, adsorption and removal of industrial dyes, heavy metals, pharmaceuticals, and corrosion inhibition on metallic surfaces. He also specializes in catalytic reactor simulation using advanced reaction models and computational fluid dynamics. With an H-index of 42 and approximately 4700 citations, Pr. Benguerba has published nearly 130 research and review articles. His expertise spans molecular modeling, process simulation, catalysis, chemical reactivity, coking, catalyst deactivation, biocatalysis, fermentation, membrane-based separations, and the design of innovative materials. His work is widely recognized in the global scientific community through numerous international conference presentations.